

Carderock Division, Naval Surface Warfare Center

West Bethesda, Maryland 20817-5700

NSWCCD-50-TR-1999/036 August 1999

Hydromechanics Directorate
Research and Development Report

Dynamic Effects on Propeller Blade Section Lift, Drag, and Pitching Moment Coefficients

by
Young T. Shen
and
Donald Fuhs



19990831 051



Approved for public release.
Distribution unlimited.

ERRATA change

5 Oct 99

Kay Adams 301-227-1612
Naval Surface Warfare Ctr
Caterock, MD
Sent in Aug

Dynamic Effect on Propeller Blade
section lift, drag, and
Pitching moments coefficients

Library # R025741

Should be NSWCCD-50-TR-1999/
1036

on RDP has CRDKN ~~SWC~~ / HD-1205-05

19990831051

A367312

REPORT DOCUMENTATION PAGEForm Approved
OMB No. 0704-0188

Public reporting burden for this collection of information is estimated to average 1 hour per response, including the time for reviewing instructions, searching existing data sources, gathering and maintaining the data needed, and completing and reviewing the collection of information. Send comments regarding this burden estimate or any other aspect of this collection of information, including suggestions for reducing this burden, to Washington Headquarters services, Directorate for Information Operations and Reports, 1215 Jefferson Davis Highway, Suite 1204, Arlington, VA 22202-4302, and to the Office of Management and Budget, Paperwork Reduction Project (0704-0188), Washington, DC 20503.

1. AGENCY USE ONLY (Leave blank)		2. REPORT DATE May 1999		3. REPORT TYPE AND DATES COVERED R & D Final	
4. TITLE AND SUBTITLE Dynamic Effects on Propeller Blade Section Lift, Drag, and Pitching Moment Coefficients				5. FUNDING NUMBERS PE: 62121N Proj No: R2332 WU: 5400-414	
6. AUTHOR(S) Young T. Shen and Donald Fuhs					
7. PERFORMING ORGANIZATION NAME(S) AND ADDRESS(ES) Naval Surface Warfare Center Carderock Division 9500 MacArthur Boulevard West Bethesda, MD 20817-5700				8. PERFORMING ORGANIZATION REPORT NUMBER CRDKNSWC/HD-1205-05	
9. SPONSORING/MONITORING AGENCY NAME(S) AND ADDRESS(ES) Office of Naval Research Ship Structures and Systems S&T Division 334 800 N. Quincy Street Arlington, VA 22217				10. SPONSORING/MONITORING AGENCY REPORT NUMBER	
11. SUPPLEMENTARY NOTES					
12a. DISTRIBUTION/AVAILABILITY STATEMENT Approved for public release; distribution is unlimited.				12b. DISTRIBUTION CODE	
13. ABSTRACT (Maximum 200 words) The Propeller Force Module (PFM) uses the blade element/momentum theory to predict propeller forces during maneuvers. A typical inflow angle distribution is studied. The blade sections will encounter spatial and temporal variations in angles of attack. Theories to calculate unsteady effects on section lift, drag, and pitching moment coefficients are formulated and presented in this report. Using the classic approach developed in aerodynamics, the section lift and pitching moment are expressed in circulatory and non-circulatory solutions. The non-circulatory solution is found to be a universal function independent of the type of motion. The circulatory solution depends heavily on the type of motion. In the case of ramp-up and ramp-down motions simulating blade sections experiencing angle of attack variations when maneuvering, an analytical solution is obtained for the circulatory lift. Empirical formula are developed to calculate the delay in stall angle due to unsteady motion. The classic aerodynamic theories assume the flow to be potential which give zero drag. Instead, Leishman's mathematical model assuming a loss of full suction pressure recovery at the leading edge due to viscous effect is adopted in this report to calculate the dynamic drag. The theories are compared with experimental measurements by Francis and Keese, and by Ham and Garelick with encouraging results.					
14. SUBJECT TERMS				15. NUMBER OF PAGES 56+vi	
				16. PRICE CODE	
17. SECURITY CLASSIFICATION OF REPORT UNCLASSIFIED		18. SECURITY CLASSIFICATION OF THIS PAGE UNCLASSIFIED		19. SECURITY CLASSIFICATION OF ABSTRACT UNCLASSIFIED	
				20. LIMITATION OF ABSTRACT SAR	

NSN 7540-01-280-5500

Standard Form 298 (Rev. 2-89)
Prescribed by ANSI Std. Z39-18
298-102

CONTENTS

NOMENCLATURE.....	v
ABSTRACT	1
ADMINISTRATIVE INFORMATION.....	1
INTRODUCTION	1
STATIC FORCE CHARACTERISTICS.....	2
STATIC LIFT	3
Fully Attached Flow Regime	3
Fully Separated Flow Regime	3
Transition Flow Regime	4
STATIC DRAG.....	4
Fully Attached Flow Regime	4
Fully Separated Flow Regime	5
Static Pitching Moment	5
UNSTEADY INFLOW AND EFFECTS ON FORCES.....	5
INFLOW DISTRIBUTIONS ON THE PROPELLER DISC.....	5
EFFECTS OF UNSTEADY MOTIONS ON FORCES.....	6
UNSTEADY FLOW THEORIES FOR DYNAMIC LIFT.....	7
CLASSIC AIRFOIL THEORIES.....	7
NUMERICAL MODELS FOR THE PFM CODE IN FULLY ATTACHED FLOW	10
Fully Attached Flow	10
Dynamic Lift Slope $\partial C_L / \partial \alpha$	12
NUMERICAL MODELS FOR THE PFM CODE IN FULLY SEPARATED FLOW	12
LIFT IN A TRANSITION FLOW REGIME	12
FLOW REGIME PREDICTION.....	13
Dynamic Lift Stall Angle α_{DLS}	13
Dynamic Moment Stall Angle α_{DM}	14
DYNAMIC LIFT : THEORY AND EXPERIMENT COMPARISON.....	14
FRANCIS AND KEESEE EXPERIMENTAL DATA	14
NUMERICAL AND EXPERIMENTAL COMPARISON.....	15
UNSTEADY FLOW THEORIES FOR DYNAMIC DRAG.....	16
FULLY ATTACHED FLOW THEORY.....	16
FULLY SEPARATED FLOW THEORY	17
DYNAMIC DRAG : THEORY VS EXPERIMENT	17
FRANCIS AND KEESEE EXPERIMENTAL DATA	17
NUMERICAL AND EXPERIMENTAL COMPARISON.....	17
Fully Attached Flow	17
Fully Separated Flow.....	18
UNSTEADY FLOW THEORIES FOR DYNAMIC PITCH MOMENT	18
DYNAMIC MOMENT : THEORY VS EXPERIMENT	19
FRANCIS AND KEESEE EXPERIMENTAL DATA	19
NUMERICAL AND EXPERIMENTAL COMPARISON.....	20
CONCLUSIONS.....	20
REFERENCES	55

TABLES

1. Dynamic vs static lift slope.	23
2. Computed and Measured Dynamic Lift.....	24
3. Dynamic Drag in an Attached Flow.	25
4. Computed Dynamic Drag in a Separated Flow.....	26
5. Moment Stall Angles and Moment Coefficients.....	26

FIGURES

1. Section lift, drag and pitch moment characteristics.....	27
2. Pressure inside a separated flow cavity as a function of foil angle.....	29
3. Force resolution on an airfoil in unsteady flow	30
4. Modeling of steady drag for nominally attached flow	30
5. Inflow angles in the propeller plane at $r/R=0.4$ for a typical turn	31
6. Approximate angles of attack in left turn.....	33
7. Effect of angle of attack on dynamic characteristics (Vertol 23010-1.58 Airfoil Section.....)	35
8. Reduced record of normal and longitudinal force for Profile B	36
9. Wagner function $\phi(s)$ and approximation	37
10. Maximum lift coefficient variation with pitch rate.....	38
11. Angle of attack for maximum lift coefficient variation with pitch rate	39
12. Force and moment characteristics: NACA 0012, $U_\infty=33.1$ ft/s.....	40
13. Steady flow lift characteristics, $k=0$	43
14. Unsteady flow	44
15. Unsteady effects on lift: experiments.....	45
16. Computed C_L (Eq. 22) including both circulatory and non-circulatory contributions vs. measurements	46
17. Computed non-circulatory C_L with $\alpha W=0$ vs. measurements.....	47
18. Ramp tests by Ham	48
19. Unsteady effects on drag force	49
20. Unsteady effects on drag theory vs. experiments	52
21. Unsteady effects on pitch moment, theory vs measurements in fully attached flow.....	53
22. Steady section force characteristics of NACA 0012 wing section	54

NOMENCLATURE

A_1, A_2, b_1, b_2	coefficients used in approximation to Wagner's function
c	blade section local chord length
$C(K)$	Theodorsen function
C_C	leading edge suction force
C_D	static section drag
C_{DF}	static friction drag
C_{DP}	static pressure drag
C_L	lift coefficient
C_{Lmax}	maximum lift coefficient
$C_{Lmax,st}$	static maximum lift
C_{Lss}	lift coefficient at static stall
C_m	dynamic pitch moment coefficient
C_N	normal force coefficient
C_P	pressure coefficient
h	vertical translation in pitching and heaving motion
K	reduced frequency, $\omega c/2U$
L	dynamic lift, see Eq. 9
M	dynamic pitch moment
P	reference pressure
P_0	cavity pressure
R	non-dimensional pitch rate $R=\alpha'c/2U$, Eq. 7
s	non-dimensional time parameter, $s=2Ut/c$
t	dimensional time
U	free stream velocity
α	angle of attack
$\alpha(0)$	initial angle of attack, see Eq (9)
α'	rate of change of angle of attack
α_{att}	angle of attack when the flow reattaches
α_{Cl0}	zero lift angle
α_{DLS}	dynamic lift stall angle

α_{DM}	dynamic moment stall angle
α_E	effective angle of attack
α_{fS}	angle of attack when the flow becomes fully separated
α_G	geometric angle of attack
α_w	time history effects of the change in α
α_{ss}	static stall angle of attack
α_0	mean foil angle
$\Delta\alpha$	oscillation frequency
ζ	recovery factor
η	a parameter to relate lift and angle of attack, see Eq. 2
σ	cavitation number (negative pressure coefficient) in a fully separated flow, see Eq. 3a
Φ	Wagner's function, approximated by Eq (7)
Ψ	azimuth angle in the transverse plane
ω	oscillation frequency
Ω	propeller rotational speed in rad/sec
Subscripts	
C	circulatory
NC	non-circulatory

ABSTRACT

The Propeller Force Module (PFM) uses the blade element/momentum theory to predict propeller forces during maneuvers. A typical inflow angle distribution is studied. The blade sections will encounter spatial and temporal variations in angles of attack. Theories to calculate unsteady effects on section lift, drag, and pitching moment coefficients are formulated and presented in this report.

Using the classic approach developed in aerodynamics, the section lift and pitching moment are expressed in circulatory and non-circulatory solutions. The non-circulatory solution is found to be a universal function independent of the type of motion. The circulatory solution depends heavily on the type of motion. In the case of ramp-up and ramp-down motions simulating blade sections experiencing angle of attack variations when maneuvering, an analytical solution is obtained for the circulatory lift. Empirical formulas are developed to calculate the delay in stall angle due to unsteady motion. The classic aerodynamic theories assume the flow to be potential which gives zero drag. Instead, Leishman's mathematical model assuming a loss of full suction pressure recovery at the leading edge due to viscous effect is adopted in this report to calculate the dynamic drag.

The theories are compared with experimental measurements by Francis and Keesee, and by Ham and Garelick with encouraging results.

ADMINISTRATIVE INFORMATION

The work described in this report was performed by the Propulsor and Fluid Systems Department of the Hydromechanics Directorate, Carderock Division, Naval Surface Warfare Center. This work was sponsored by the Office of Naval Research, Ship Structures and Systems S&T Division (Code 334), program 62121N, project number R2332, work unit 5400-414.

INTRODUCTION

The Propeller Force Module (PFM) [1] has been developed by Analytical Methods Inc. (AMI) to predict propeller forces in maneuver, such as turning or crashback. The PFM is a blade element code that executes quickly because the blade section lift, drag and pitching moment coefficients are determined off-line and stored in a look-up table.

The sample cases provided by AMI used the XFOIL code [2] developed by MIT to calculate the 2-D section lift and drag coefficients up to the stall angle. Beyond the static stall angle, the experimental data [3] of the NACA 0012 foil are used regardless of the propeller blade section geometry.

An alternative method to calculate blade section coefficients including camber effect at a backing condition was developed by Jiang*. These coefficients are calculated from an engineering

* Jiang, C.W., "Foil Sectional Lift, Drag, and Moment Coefficients Preparation for Propeller Force Module (PFM) Input", NSWCCD internal memorandum (December 1996).

approach that includes the use of the MIT's potential flow code PSF-10. Since the PSF-10 code is a three-dimensional program, a large aspect ratio foil is used. The section forces at mid-span are calculated to generate two-dimensional force coefficients. Beyond the static stall angle, a semi-empirical formula is used to cover the whole range of angles of attack.

The current propeller blade section coefficients developed by Jiang and Reference [1] are based on steady state data. With the propeller operating behind a ship stern, the propeller blade sections will encounter different inflow angles onto the propeller blades at different azimuth angles due to spatial variation in ship hull wake. Maneuvering conditions further change the ship wake in the propeller plane. The blade sections will encounter spatial and temporal variations in inflow angles. Unsteady effects on forces can be quite substantial [4].

The existing PFM code uses the blade element theory to determine blade section forces from a predetermined table of foil characteristics. However, in the unsteady case, the force is sensitive to the unsteady parameters, such as reduced frequency, and the type of foil motion, such as in a pitching and heaving motion or in a gust field, or a step change in foil angle with time, etc. Extremely large numbers of tables are needed to calculate the section forces to cover different flow parameters.

An important consideration in the development of any hydrodynamic prediction method is its use in conjunction with other calculations in the simulation code. Simulations require predicting hull forces and moments and propeller inflow as well as propeller forces. If the unsteady method and dynamic stall prediction method are a frequently accessed subroutine in the PFM code, then the hydrodynamic prediction method should not have large computational requirements. This objective can be met by using semi-empirical dynamic models that rely on the reconstruction of the important dynamic flow features. A RANS code can be used to provide continuous improvement of the semi-empirical models.

Time scale is a major physical parameter in a dynamic model to distinguish itself from a static model. The static data corresponds to the limiting case of unsteady forces as the non-dimensional time parameter such as the reduced frequency, K approaching zero. The study of dynamic forces can be treated as an extension of the static forces [4]. Static data will be used extensively in developing this dynamic model. Previously, a dynamic model was developed for lift [4]. The present report develops dynamic models for drag, pitching moment, and non-circulatory lift while summarizing the circulatory lift model.

STATIC FORCE CHARACTERISTICS

Typical static lift, drag, and pitching moment coefficients of NACA section profiles are shown in Fig. 1 at several propeller radii. A major distinction between a cambered foil and a symmetric foil is the shift in the value of the zero lift angle. Aside from that, the basic force characteristics with respect to the foil angles between symmetric and cambered foils are similar. The following discussions are applicable to symmetric foils as well as cambered foils.

STATIC LIFT

The static lift characteristics are shown in Fig. 1a. At low angles of attack, the flow on the foil surface is fully attached. As angles are increased, at some critical angle, the boundary layer on the foil surface begins to experience flow separation. At this foil angle, the pitch moment coefficient shows an abrupt change. This critical angle is termed the static moment stall angle, α_{SM} . Further increase in foil angle results in a sharp drop in lift. The foil is in static stall. This foil angle is termed the static lift stall angle or often termed the static stall angle, α_{SS} . A further increase in foil angle results in a full flow separation.

Fully Attached Flow Regime

Between the foil angles at Points 1 and 3 of Fig. 1, the flow is fully attached. The lift is seen to increase linearly with the foil angle. The static lift is related to the foil angle by

$$C_L = \left(\frac{\partial C_L}{\partial \alpha} \right) \alpha \quad \alpha < \alpha_{SS} \quad (1)$$

where α denotes the effective angle. For a cambered foil α is given by $\alpha = \alpha_G + \alpha_{Cl=0}$, the geometric angle of attack plus zero lift angle. The zero lift angle is determined from experimental data as given in Fig. 1a or calculated from a RANS code. For a symmetric foil, the zero lift angle is zero and the effective foil angle is given by the geometric angle of attack α_G .

For a 2-dimensional foil, the lift slope can be expressed by

$$\partial C_L / \partial \alpha = 2 \pi \eta \quad \alpha < \alpha_{SS} \quad (2)$$

Depending on the Reynolds number and the section profile such as thickness and camber distributions, the value of η varies around 0.95 to 0.97. In this report the value of η is determined from experimental data such as Fig. 1a.

Fully Separated Flow Regime

For a foil angle between the Points 5 and 6 of Fig. 1, the flow on the upper surface is fully separated. Let α_{FS} denote the angle at Point 5, which is the inception angle for flow to be fully separated. The lift again is seen to increase almost linearly with the foil angle but with a much smaller value of lift slope than the attached case. It is shown in Ref [4] that the lift in a fully separated flow can be approximated by the following formula. Let σ denote the non-dimensional pressure coefficient inside the separated flow (cavity) and given by

$$\sigma = -C_p = \frac{(P_0 - P)}{0.5 \rho U^2} \quad (3a)$$

where P and P_0 denote cavity pressure and reference pressure, respectively. For a small value of σ the lift coefficient is given by

$$C_L = \frac{2\pi \sin \alpha}{4 + \pi \sin \alpha} \left[1 + \sigma + \frac{\sigma^2}{8(\pi + 4)} \right] \cos \alpha \quad \alpha > \alpha_{fs} \quad (3b)$$

The intensity of the cavity pressure inside the separated flow depends on the intensity of vortex generated in the free shear layer, which in turn is a function of the foil angle. The cavity pressure in terms of foil angle is shown in Fig. 2. It is shown in Ref [4] that the measured lift forces in a separated flow are well predicted by Eq. 3.

Transition Flow Regime

The flow patterns at the foil angles between Points 4 and 5 are very complex and unstable. The flow is in a transition stage between a fully attached flow and fully separated flow. The location of the flow separation point is sensitive with the hydrodynamic parameters, such as Reynolds number and profile shape. Empirical formulas, to be outlined later, will be used to relate the lift force with the foil angle in this transition flow regime.

STATIC DRAG

In an ideal fluid, a two dimensional foil has zero drag. In a real fluid the foil will experience friction and pressure drag. A static section drag coefficient C_D can be expressed in terms of static friction drag C_{DF} and static pressure drag C_{DP} as follows

$$C_D = C_{DF} + C_{DP} \quad (4)$$

The drag coefficient is dominated mainly by the friction drag at a low angle of attack and by the pressure drag at a high angle of attack. It is assumed that the influence of foil angle on friction drag is small [5]. The friction drag is determined from experimental data at the zero angle of attack. On the other hand, the pressure drag is very sensitive to the foil angle. A theory to predict pressure drag is presented in this report. This formula will be extended to develop a theory for dynamic drag. Similar to the lift case, the formula to compute the pressure drag depends on the flow regime.

Fully Attached Flow Regime

Leishman [5,6] shows that the pressure drag is related to the leading edge suction force (the chord force) as sketched in Fig. 3. In a fully attached flow the lift is given by $\rho V \Gamma$, where Γ denotes the circulation. Let C_N and C_C denote the normal force and the leading edge suction force. In an ideal fluid the drag force is zero as the lift in the streamwise component is balanced by the leading edge suction force. In a real fluid the suction force does not recover 100 % of the lift component and pressure drag is induced. Let ξ denote the recovery factor. Mathematically, the pressure drag in terms of recovery factor can be expressed by [5]

$$C_{DP} = C_N \sin \alpha - \xi C_C \cos \alpha = 0.5 C_L (1 - \xi) \sin 2\alpha \quad (5)$$

Fig. 4 taken from Ref [5] shows the comparison of this theory and measurements of the NACA 0012 foil with $\xi = 0.97$. The agreement between computations and measurements is very good for angles less than stall. Additional drag measurements of the NACA 0012 foil at three Reynolds numbers of 3.0, 6.0 and 9.0×10^6 are given in page 463 of Ref [7]. Good agreement between the above theory and measurements are obtained when $\xi = 0.96, 0.97$ and 0.974 are used for the Reynolds numbers of 3.0, 6.0 and 9.0×10^6 respectively. As noted in Ref [5], a typical value of ξ is around 0.95 to 0.97.

Fully Separated Flow Regime

It is shown in Ref [4] that the foil drag in a separated flow is well predicted by the following formula.

$$C_{DP} = \frac{2\pi \sin \alpha}{4 + \pi \sin \alpha} \left[1 + \sigma + \frac{\sigma^2}{8(\pi + 4)} \right] \sin \alpha \quad (6)$$

Since flow is only attached on the lower surface with flow on the upper surface separated, only half of the friction drag given in Eq. 4 is to be used. In practice, the friction drag is so small when compared with the form drag in a separated flow that the friction drag can be neglected.

Static Pitching Moment

A thin wing theory shows that the resultant lift acts at the quarter chord. Moment along the quarter chord is zero. However, due to thickness and camber effects, pitch moment coefficients along the quarter chord can differ from zero. In the present mathematical model, experimental data will be used to obtain the static pitch moment coefficient.

UNSTEADY INFLOW AND EFFECTS ON FORCES

INFLOW DISTRIBUTIONS ON THE PROPELLER DISC

Figs 5a and 6a show typical inflow angles in the propeller plane at 0.4 and 0.7 propeller radii for a ship in a turn. The vertical axis denotes the inflow angle $\alpha = \phi - \beta$, where ϕ and β denote geometric pitch angle and hydrodynamic angle. A blade section will experience large variation of inflow angle as much as plus and minus 15 to 16 degrees in every cycle of propeller rotation as noted in Figs 5 and 6.

The shapes of inflow angle distribution are quite different from a sinusoidal. Instead, the inflow angle distribution can be reasonably approximated by dividing into 17 straight line segments as shown in Fig. 5b. For examples, the angle of attack increases linearly with time at the segment between Points 2 and 3, and decreases linearly with time between Points 4 and 5 of Fig. 5b. This type of motion at each segment is similar to a ramp-up and down motion of a constant pitch rate. It is noted that the azimuth angle is related to time from the propeller RPM. The shape of the inflow angle distribution at Fig. 6a is also reasonably represented by 17 straight lines.

The juncture between two adjacent segments will experience Wagner type step change in foil angle [8].

EFFECTS OF UNSTEADY MOTIONS ON FORCES

Airfoils in a sinusoidal motion have been extensively investigated both theoretically and experimentally. Force measurements on an airfoil under a sinusoidal pitching oscillation are shown in Fig. 7 [9]. The reduced frequency in this test program was 0.062. The oscillation amplitude was kept at a constant value of 4.85 degs. But the mean angles were varied to examine the force characteristics in different flow regimes.

Fig. 7 shows that (1) The dynamic stall angle of 16 deg is higher than the static stall angle of 13 degs even at this low reduced frequency. (2) The difference in dynamic and static lift coefficient is noticeable at the same foil angle. As an example, at the angle of attack of 15 degs, the dynamic lift coefficient is around 1.6 while the static lift coefficient is around 0.99. An increase in lift by 60 % is observed due to the unsteady motion. (3) The slope of the dynamic lift curve with foil angle is almost parallel to the static curve both in fully attached flow regime and fully separated flow regime. These observations are important because a few assumptions to be used in developing the present dynamic model are based on these observations.

The second example is an airfoil experiencing ramp-up and ramp-down motions [10]. Recall Fig. 5a. The propeller blades passing through Points 2, 3, 4 and 5 will experience unsteady motion similar to a ramp motion. To characterize this type of unsteady motion a nondimensional pitch rate, R is defined by

$$R = \alpha'c/2U \quad (7)$$

where c , U and α' denote foil chord, free stream velocity, and the time derivative of instantaneous foil angle. Unless explicitly stated, the unit α' used in this report is radian per second. Seven models consisting of two symmetric and five cambered airfoils were tested by Farren [10]. One of the test results is shown in Fig. 8. The x-axis denotes the instantaneous foil angle. The y-axis denotes the lift coefficient K_z , normalized by $\rho c U^2$; namely K_z in Fig. 8 is one half of the conventional lift coefficient C_L .

Two sets of test data are shown in Fig. 8. The first set of tests were conducted with the foil angles increased slowly ($\alpha' \uparrow$ slow), and then decreased slowly ($\alpha' \downarrow$ slow). The second set of tests were conducted with the foil angles increased and decreased at a faster pitch rate of 1 deg in 2.5 chords. This type of motion is very similar to the change of inflow angle distribution on the propeller blades as observed in Figs 4 and 5. Studies of Farren's test data lead to the development of dynamic models to be presented later in this report. The lift response to this type of motion in a fully attached flow and a fully separated flow are examined.

First, consider the measured lift at the angle of attack of 10 deg. As noted in Fig. 8, the flow at this angle is expected to be fully attached. The lift coefficient C_L of 1.44 ($K_z = 0.72$) is measured at 10 degs when the foil angle is increased at a faster pitch rate ($\alpha' \uparrow$ fast). At the same

foil angle the measured lift coefficient is 1.38 ($\alpha \uparrow$ slow) at a slow pitch rate. The lift at a fast and a slow pitch down motion are 1.27 ($\alpha \downarrow$ slow) and 1.15 ($\alpha \downarrow$ fast), respectively. In addition to the delay in stall, a difference of 25 % in lift is observed at the same foil angle. Note that the pitch rates used in these series of tests are small when it is compared with the pitch rates to be experienced in Figs 5 and 6. Furthermore, it is noted that the dynamic lift is higher with an increasing pitch rate ($\alpha \uparrow$) than with a decreasing pitch rate ($\alpha \downarrow$) for the foil at the same angle of attack.

Next, consider the test case with the flow fully separated, say at 30 degs. The measured lift coefficients C_L are 1.53 ($\alpha \uparrow$ fast), 1.40 ($\alpha \uparrow$ slow), 1.34 ($\alpha \downarrow$ slow) and 1.27 ($\alpha \downarrow$ fast), respectively. A difference of 20 % in lift due to unsteady motion is observed at the same foil angle with the flow fully separated.

Unsteady effect on lift is seen to be quite substantial in this type of motion whether the flow is fully attached or fully separated. The lower the static lift coefficient, the greater the difference in lift percentage-wise from the unsteady motion. For a typical static blade section design lift coefficient of 0.2 to 0.3, the difference in dynamic lift vs static lift can be significant, greater than 20 to 25 % as noted in this example. As to be discussed in the later part of this report, the change of pitch rates used in this series of tests is small when compared with the change of pitch rates given in Figs 5 and 6. A significant unsteady effect on force characteristics is to be expected.

UNSTEADY FLOW THEORIES FOR DYNAMIC LIFT

CLASSIC AIRFOIL THEORIES

The concern of airfoil flutter and divergence problems lead to the development of the Theodorsen function [11] in sinusoidal pitching and heaving motion. The unsteady problem of an airfoil in a transverse gust is solved by Sears [12]. The problem of a step change in foil angle is solved by Wagner [8]. The problem of a sharp edged gust striking the leading edge of the airfoil is solved by Kussner [13].

The classic Theodorsen's solution is summarized as following. Consider an airfoil with the chord length equal to $2b$ and moving in vertical translation $h(t)$ and rotating about an axis at $x = ab$ through an angle $\alpha(t)$, where t denotes time. Let ω , α_0 and $\Delta\alpha$ denote oscillation frequency, mean foil angle and oscillation amplitude, respectively. Let $\alpha(t)$ denote the instantaneous foil angle and is given by

$$\alpha(t) = \alpha_0 + \Delta\alpha \sin \omega t \quad (8)$$

Let K denote the reduced frequency by $K = \omega c/2U$. The dynamic lift can be expressed by [14]

$$L = \pi \rho b^2 (h'' - ba\alpha'') + \pi \rho b^2 U \alpha' + 2\pi \rho U b C(K) [h' + U\alpha + b(\frac{1}{2} - a)\alpha'] \quad (9)$$

where ' and '' denote first and second derivatives with time. $C(K)$ denotes the Theodorsen function.

The α' term is known to be circulatory, but the coefficient is a constant and independent of reduced frequency. Eq. 9 can be expressed with circulatory L_C and non-circulatory L_{NC} parts [14].

$$\begin{aligned} L &= L_{NC} + L_C \\ &= \pi \rho b^2 (h'' - ba \alpha'' + U \alpha') \\ &\quad + 2\pi \rho U b C(K) [h' + U \alpha + b(1/2 - a) \alpha'] \end{aligned} \quad (10)$$

The α' term is now treated in the non-circulatory solution.

The gust problem has the same identical non-circulatory solution as given in Eq. 10 but has a different circulatory solution. It was pointed out by Bisplinghoff, Ashley and Halfman [14] that the non-circulatory solution is the same regardless of the nature of motion as long as it is small. On the other hand, the circulatory flow solution is motion dependent. This means that the dynamic solution with respect to any type of motion has the same non-circulatory solution as given in Eq. 10 but has a unique solution for each type of motion. This important observation will be used extensively in developing the present dynamic model.

A typical inflow angle distribution for the present study is given in Figs. 5 and 6. Instead of using the solutions from a sinusoidal motion, Wagner's step change in foil angle approach may be more applicable to the motion to be encountered by a propeller with the inflow angle distribution given in Fig. 5 or 6. Let $\Delta\alpha$ denote the step change in angle of attack. The solution of circulatory lift is given by Theodorsen [11]

$$L_C = 2\pi \rho U^2 b \Delta\alpha \phi(s) \quad (11a)$$

or
$$C_{LC} = (\partial C_L / \partial \alpha) \Delta\alpha \phi(s) \quad (11b)$$

where $s = 2Ut/c$. $\phi(s)$ is the Wagner function as shown in Fig. 9. Note that $\phi(0) = 0.5$. This means that only half of the lift is generated at that instant of time $t = 0$.

Recall Fig. 5. Instead of a step change in angle of attack, the inflow angle distribution is more closely related to a continuous increase or decrease in angle of attack with time. This type of motion will be treated like a series of step changes in angle of attack. In this kind of motion, the angle of attack varies across the chord, namely the blade section has different angles of attack at the leading edge, mid-chord, and trailing edge at the same instant of time. Let $w_{3/4 C}$ denote the vertical component of velocity at the three-quarter chord, namely $w_{3/4 C} = -U\alpha$.

Consider a case where the foil experiences a step change in angle of attack at time $t = 0$. Based on the superposition integral, the dynamic lift on an airfoil starting from rest at $t = 0$ and experiencing a continuous change in foil angle with time is given by

$$\begin{aligned} L &= L_{NC} + L_C \\ &= \pi \rho b^2 (h'' - b a \alpha'' + U \alpha') \\ &\quad - 2\pi \rho U b \left[w_{\frac{3}{4}c}(0) \phi(s) + \int_0^s dw_{\frac{3}{4}c}(u) / du \phi(s-u) du \right] \end{aligned} \quad (12a)$$

The circulatory lift can be expressed by

$$C_{LC} = \partial C_L / \partial \alpha [\alpha(0) \phi(s) + \int d\alpha(u)/du \phi(s-u) du] \quad (12b)$$

In a real-time simulation study, the above convolution integral is often approximated by the following numerical scheme [15, 16]. Note that physically, the Wagner function represents time required for the foil to attain the steady lift. The circulatory lift can be calculated by introducing a parameter termed effective angle of attack $\alpha_E(s)$ by

$$C_{LC} = (\partial C_L / \partial \alpha) \alpha_E(s) \quad (13)$$

where

$$\alpha_E(s) = \alpha(0) \phi(s) + \int d\alpha/du \phi(s-u) du \quad (14)$$

Beddoes [15] presents the following numerical approximation to Duhamel's integral for the effective angle.

$$\alpha_E(s) = \alpha(0) \phi(s) + \sum_{n=1}^m \Delta \alpha_n - X_n - Y_n \quad (15)$$

where

$$X_0 = 0 \quad \text{and} \quad X_n = X_{n-1} e^{-b_1 \Delta s} + A_1 \Delta \alpha_n \quad (16a)$$

and

$$Y_0 = 0 \quad \text{and} \quad Y_n = Y_{n-1} e^{-b_2 \Delta s} + A_2 \Delta \alpha_n \quad (16b)$$

The constants A_1 , A_2 , b_1 , and b_2 are 0.165, 0.335, 0.0455 and 0.3, respectively [15].

NUMERICAL MODELS FOR THE PFM CODE IN FULLY ATTACHED FLOW

Fully Attached Flow

Eq. 13 is used extensively in the helicopter industry [15, 16]. This method still requires a substantial amount of computation time. A method to compute section forces in propeller blades is a frequently accessed subroutine in the PFM code, so a simple method will be developed to evaluate this convolution integral. The Wagner function has a complicated mathematical form. However, a simple formula has been found to approximate the Wagner function with reasonable accuracy [14].

$$\phi(s) = (s + 2) / (s + 4) \quad (17)$$

Fig. 9 shows a comparison of the numerical results obtained from Eq. 17 vs the exact Wagner function.

As noted in Fig. 5., the rate of change in the angle of attack at the azimuth angle $\psi = 0$ is relatively small. A steady flow condition is assumed at $\psi = 0$. Eq. 14 can be expressed by

$$\begin{aligned} \alpha_E(s) &= \alpha_0 \phi(s) + \int_0^s d\alpha / du \phi(s-u) du \\ &= \alpha_0 + \left[\int_{s_0}^{s_1} + \int_{s_1}^{s_2} + \dots + \int_{s_{n-1}}^{s_n} d\alpha / du \phi(s-u) du \right] \end{aligned} \quad (18a)$$

where $s_0 = 0$, and $s_n = s$. Numerical studies have shown that the calculations converge more quickly when the first term in Eq. 18a, $\alpha_0 \phi(s)$ is replaced by α_0 . This has the effect of neglecting circulatory effects for the initial starting transient. The convolution integral is divided into n segments by the increment

$$\Delta s = s / n, \quad s_i = i \Delta s, \quad i = 1, 2, \dots, n$$

The rate of change of angle of attack $(d\alpha/ds)_i$ is assumed to be constant between time steps.

$$\int_{s_i - \Delta s}^{s_i} d\alpha / du \phi(s-u) du = (d\alpha/ds)_i \int_{s_i - \Delta s}^{s_i} \phi(s-u) du \quad (18b)$$

Let

$$\begin{aligned} v &= s - u \\ dv &= -du \end{aligned}$$

then,

$$\begin{aligned} \int \phi(s-u) du &= - \int \phi(v) dv \\ &= - \int \frac{v+2}{v+4} dv \end{aligned}$$

$$= 2 \log(s - u + 4) - s + u \quad (18c)$$

Therefore

$$\begin{aligned} \int_{s_i - \Delta s}^{s_i} \phi(s - u) du &= [2 \log(s - u + 4) - s + u] \\ &= \Delta s + 2 \log[1 - \Delta s / (s - s_i + \Delta s + 4)] \end{aligned} \quad (18d)$$

So

$$\begin{aligned} \alpha_E(s) &= \alpha_0 + \sum_{i=1}^n \Delta s (d\alpha / ds)_i + 2 \sum_{i=1}^n (d\alpha / ds)_i \log[1 - \Delta s / (s - s_i + \Delta s + 4)] \\ &= \alpha(s) + 2 \sum_{i=1}^n (d\alpha / ds)_i \log[1 - \Delta s / (s - s_i + \Delta s + 4)] \end{aligned} \quad (19)$$

Where

$$\sum_{i=1}^n \Delta s (d\alpha / ds)_i = \alpha(s) - \alpha_0$$

Let α_w denote the last term in Eq. 19.

$$\alpha_E = \alpha - \alpha_w \quad (20a)$$

$$\alpha_w(s) = -2 \sum_{i=1}^n (d\alpha / ds)_i \log[1 - \Delta s / (s - s_i + \Delta s + 4)] \quad (20b)$$

Physically, the term α_w accounts for the time history effects of the change in α . Recall that the parameter s is related to t by $s = 2Ut/c = 2U\psi/c\omega$, from ψ equal 0 to 2π .

The dynamic lift is given by

$$\begin{aligned} C_L &= C_{LC} + C_{LNC} \\ &= (\dot{C}_L)_{static} - (\partial C_L / \partial \alpha) \alpha_w(s) + Sgn(\alpha') \pi R \end{aligned} \quad (21)$$

where

$$Sgn(\alpha') = \begin{cases} 1 & \text{if } \alpha' \text{ is positive} \\ -1 & \text{if } \alpha' \text{ is negative} \end{cases}$$

The term R is the pitch rate defined in Eq. 7.

Dynamic Lift Slope $\partial C_L / \partial \alpha$

An extensive data set on lift slope has been compiled by McLaughlin [17]. Table 1 compares the dynamic lift slope vs the static slope for several airfoil profiles with and without camber. The dynamic lift slope is seen to be a few percent lower than the static lift slope. Approximately,

$$(\partial C_L / \partial \alpha)_{\text{dynamic}} = 0.94 (\partial C_L / \partial \alpha)_{\text{static}}$$

Depending on whether the angle of attack is greater or less than the static stall angle, Eq. 20 is expressed by

$$C_L = \begin{cases} (C_L)_{\text{static}} - 0.94 (\partial C_L / \partial \alpha)_{\text{static}} \alpha_w(s) \\ + \text{Sgn}(\alpha') \pi R & \alpha < \alpha_{ss} \end{cases} \quad (22a)$$

$$\begin{cases} [(C_L)_{ss} + (\partial C_L / \partial \alpha)_{\text{static}} (\alpha - \alpha_{ss})] \\ - 0.94 (\partial C_L / \partial \alpha)_{\text{static}} \alpha_w(s) + \text{Sgn}(\alpha') \pi R & \alpha_{ss} < \alpha < \alpha_{DM} \end{cases} \quad (22b)$$

NUMERICAL MODELS FOR THE PFM CODE IN FULLY SEPARATED FLOW

To operate an airfoil in a fully separated flow is not desirable. Theoretical and experimental works on this subject are hard to find. Following the approach developed in the fully attached flow case, it is assumed that the dynamic circulatory lift has the same form as the static lift given in Eq. 3. It is further assumed that the non-circulatory lift obtained in a fully attached flow is applicable to a separated flow. The dynamic lift is then given by

$$C_L = C_{LC} + C_{LNC}$$

$$= \frac{2\pi \sin \alpha}{4 + \pi \sin \alpha} \left[1 + \sigma + \frac{\sigma^2}{8(\pi + 4)} \right] \cos \alpha + \text{Sgn}(\alpha') \pi R \quad (23)$$

LIFT IN A TRANSITION FLOW REGIME

Consider Fig. 7. The region between Points 3 and 5 is termed transition flow regime. Due to the unsteady motion, the maximum dynamic lift can be 2 to 3 times higher than the maximum lift measured in a steady case. The flow is complex and unstable in this flow regime. No theoretical treatment is available on this subject. Empirical formula will be developed to calculate the maximum lift in this transition flow regime.

Data measured by Francis and Keesee [18] cover a wide range of pitch rates. This set of data is used for this study. The non-dimensional pitch rate R is termed reduced frequency in Francis and Keesee's paper. The measured maximum lift coefficients, $C_{L_{\max}}$ vs the reduced

frequencies are given in Fig. 10. The maximum lift increases sharply at low frequencies. At high frequencies, the growth of maximum lift in terms of frequency is more gradual than the case of low frequencies. Test data [19, 20, 21] all show the same trend that the growth rate is much higher at low frequencies and flatten out at high frequencies. Johnson [21] assumes that when the lift coefficient reaches a maximum value of 3.0, the lift coefficient then remains at 3.0 as long as the foil angle is still rising. Johnson's assumption is based only on a few data points and at a relatively limited range of reduced frequencies. Data presented by Francis and Keesee cover much wider frequency range and is used to derive the following empirical formula.

Based on Fig. 10, the rate of growth in C_{Lmax} vs frequency is divided into two lines with the juncture point assigned at $R = 0.03$. The maximum lift obtained from curve fit gives

$$C_{Lmax} = \begin{cases} C_{Lmax)st} + 26.3 R & R < 0.03 \\ [C_{Lmax)st} + 0.79] + 4.78 [R - 0.03] & R > 0.03 \end{cases} \quad (24)$$

Where $C_{Lmax)st}$ denotes the static maximum lift. In addition to the NACA 0012 foil, Fig. 10 also includes NACA 64A012. Both airfoils give similar results in terms of maximum lift vs frequency. It is assumed that Eq. 24 is not sensitive with the airfoil profiles.

FLOW REGIME PREDICTION

The lift force vs foil angle exhibits different characteristics in different flow regimes, so are the theories required to predict the dynamic lift. The flow regime must be known in priori before the proper theory is applied. Since the section forces are expressed in terms of foil angles, the flow region can be classified by the using angle of attack as a parameter.

Consider Fig. 1. Between the region marked by Points 1 and 3, the flow is fully attached. When the foil angle approaches the value of Point 3, the stall vortex starts to appear at the foil leading edge. The stall vortex detaches from the leading edge at Point 3 and approaches the trailing edge at Point 4. The coherent stall vortex induces an additional suction pressure on the foil surface, especially at the rear part of the foil. The induced suction pressure results in an increase in maximum attainable lift with nose down pitching moment, and pressure drag. The pitching moment at Point 3 begins to diverge from the fully attached flow value. Point 3 is termed dynamic moment stall angle α_{DM} . Point 4 is termed dynamic lift stall angle α_{DLS} . Flow is fully separated when the foil angle is greater than the value at Point 5.

Dynamic Lift Stall Angle α_{DLS}

Angle of attack for maximum lift coefficients vs frequency is shown in Fig. 11 for NACA 0012 and NACA64A012 profiles [18]. An empirical formula to relate angle of attack α_{DLS} (deg) with reduced frequency is given as follows:

$$\alpha_{DLS} = \begin{cases} \alpha_{ss} + 460 R & R < 0.03 \\ \alpha_{ss} + 13.8 + 48.8 (R - 0.03) & R > 0.03 \end{cases} \quad (25)$$

Dynamic Moment Stall Angle α_{DM}

Let α_{ss} denote the static stall angle. Based on oscillating foil tests [20, 21] and ramp-up tests [18, 22], an empirical formula for α_{DM} (deg) is given as follows:

$$\alpha_{DM} = \begin{cases} \alpha_{ss} + 340 R & R < 0.03 \\ \alpha_{ss} + 10.2 + 53.5 (R - 0.03) & R > 0.03 \end{cases} \quad (26)$$

DYNAMIC LIFT : THEORY AND EXPERIMENT COMPARISON

FRANCIS AND KEESEE EXPERIMENTAL DATA

The unsteady lift, drag, pitching moment, and instantaneous foil angle of a NACA 0012 foil tested by Francis and Keese [18] are shown in Figs 12a, b, and c for the reduced frequencies of $R=0.047$, 0.089 , and 0.130 , respectively. The model was fabricated with a rectangular planform of 14 in (36 cm) span and 6 in (15 cm) chord which gives the aspect ratio of $AR = 2.3$. The tests were conducted in a wind speed of 33 ft/sec which gives the corresponding Reynolds number around 97,000. The steady lift characteristics are shown in Fig. 13.

First, consider the test case shown in Fig. 12a at the reduced frequency of $R = 0.047$. Except at the end points, the instantaneous foil angle is seen to increase linearly with time. This is a motion with a constant pitch rate. To facilitate further discussions, the enlarged dynamic lift curves are given in Fig. 14. The dynamic lift is seen to increase sharply at the onset of motion then increases almost linearly with the foil angle (with some wiggling). The steady data given in Fig. 13 are also plotted in Fig. 14 for comparison.

At the same foil angle, the dynamic lift is seen to be higher than the static value. The static stall occurs around the foil angle of 0.242 rad (13.8 deg). Dynamic stall occurs around 0.52 rad (29.8 deg). Stall is greatly delayed by the ramp-up motion. At a foil angle greater than 13.8 deg, the dynamic lift is substantially higher than the static lift. For an example, the static lift is 0.47 at the angle of attack of 0.3 rad (17 deg). At the same angle of attack, the dynamic lift is 1.54 at the pitch rate of 0.13 . A difference of 327% in lift coefficient is observed. This fact clearly shows that the lift determined without considering the dynamic effect can be subject to a great error. The moment stall occurs around 0.4 rad. The shape of pitch moment coefficient vs angle of attack is greatly influenced by the moment stall angle as to be shown later in this report.

The same phenomena discussed in Fig. 12a are also observed in Figs 12b and 12c at higher frequencies of $R = 0.089$ and 0.130 . Additionally, the dynamic lift and stall angles are further amplified by the unsteady motion at higher frequencies.

For further discussions, the dynamic lift coefficients taken from Fig. 12 at angles of attack of $0.1, 0.2, 0.3$ and 0.4 rad are plotted in Fig. 15. The dynamic lift increases with frequency (pitch rate). It is somewhat surprising to see that the dynamic lift curves at different pitch rates are almost parallel to each other. Furthermore, at angles of attack less than the static stall angle of 0.24 rad, the dynamic lift curves are almost parallel to the static lift curve. These results agree with McLaughlin's data given in Table 1. Fig. 15 supports the assumption given in Eq. 21.

NUMERICAL AND EXPERIMENTAL COMPARISON

The computed lift from Eq. 22 will now be compared with measurements. Fig. 13 gives the static lift slope of 3.4 and the static stall angle of 2.42 rad. Fig. 12 provides the relationship between the instantaneous angle and time. The nondimensional time s is computed by $s = 2Ut/c$, where U is 33.1 ft/sec and c is 0.5 ft in this series of model tests. The computed results are given in Table 2a, b, c, and d for $\alpha = 0.1, 0.2, 0.3$, and 0.4 rad.

The dynamic lift computed from Eq. 22 is shown in Fig. 16. The dynamic value over the static value is enhanced by the non-circulatory lift $\text{Sgn}(\alpha') \pi R$ but reduced by the circulatory lift $(\partial C_L / \partial \alpha)_{\text{static}} \alpha_w(s)$ due to the time history effect of the change in angle of attack. Because of the reduction in circulatory lift, the computed values are smaller than the measured values, especially at large angles of attack. Recall Fig. 14. In this test series, the dynamic lift increases sharply and reaches full static lift in less than 0.05 sec. The test results seen in Fig. 14 indicate the reduction in circulatory lift is relatively small. The computed dynamic lift is shown in Fig. 17 with the reduction in circulatory lift set to zero, namely $\alpha_w = 0$. The computed dynamic lift with $\alpha_w = 0$ is seen to agree well with the measurements.

Recall that the non-circulatory lift is independent of motion. To include this term in dynamic calculation is correct. The circulatory lift is motion dependent. The theory predicts a substantial drop in lift due to the time history effects of the change in α . It is not clear why a strong time history effect on lift is not observed experimentally.

Another example is shown in Fig. 18 [23]. The model is made of a NACA 0012 airfoil. The instantaneous foil angle and time history is shown in Fig. 18a. The dynamic lift and static lift are shown in Fig. 18b. For angles less than the static stall angle the dynamic lift curve is seen to be parallel with the static lift curve. This result is in agreement with Fig. 15.

The pitch rate shown in Fig. 18a is around $R = 0.023$. The computed dynamic lift with $\alpha_w = 0$ is given in Table 2 and also plotted in Fig. 18b for comparison. The computed values are slightly smaller than the measured values. However, the trend of lift vs angle of attack is correctly predicted.

UNSTEADY FLOW THEORIES FOR DYNAMIC DRAG

A section drag coefficient C_D can be expressed in terms of friction drag C_{DF} and pressure drag C_{DP} as follows.

$$C_D = C_{DF} + C_{DP} \quad (4)$$

Friction drag on an oscillating airfoil in a fluctuating free stream has been studied by Kottapalli and Pierce [24]. These data were further analyzed by Leishman [6] who shows that unsteady viscous drag fluctuations are generally quite small and negligible when compared with the pressure drag. It is assumed that friction drag is not frequency dependent.

$$(C_{DF})_{dynamic} = (C_{DF})_{static} \quad (27)$$

This assumption implies that the unsteady effect on the drag force comes from the pressure drag. Dynamic effect on pressure drag is computed as follows.

FULLY ATTACHED FLOW THEORY

Let the normal force C_N to be expressed by the circulatory and non-circulatory flow components C_{NC} and C_{NNC} .

$$C_N = C_{NC} + C_{NNC} \quad (28)$$

The dynamic pressure drag due to a change in angle of attack can be expressed by

$$\begin{aligned} C_{DP} &= C_N \sin \alpha - \xi C_C \cos \alpha \\ &= (C_{NC} \sin \alpha - \xi C_C \cos \alpha) + C_{NNC} \sin \alpha \end{aligned} \quad (29)$$

The terms inside the parenthesis represent the circulatory flow solution. As shown in the dynamic lift solution, the circulatory flow solution can be replaced by the static term,

$$C_{NC} \sin \alpha - \xi C_C \cos \alpha = 0.5 C_L (1 - \xi) \sin 2\alpha \quad (30)$$

Note that $C_N = C_L \cos \alpha$ (see Fig. 3). The non-circulatory flow solution C_{NNC} is replaced by $Sgn(\dot{\alpha}) \pi R \cos \alpha$.

The dynamic drag in a fully attached flow can be expressed by

$$\begin{aligned}
C_D &= C_{DF} + C_{DP} \\
&= [C_{DF} + 0.5 C_L (1 - \xi) \sin 2\alpha]_{static} \\
&\quad + \text{Sgn}(\alpha') \pi R \cos \alpha \sin \alpha \quad \alpha < \alpha_{ss} \quad (31a)
\end{aligned}$$

$$\begin{aligned}
C_D &= [C_{DF} + 0.5 [(C_L)_{ss} + (\partial C_L / \partial \alpha)_{static} (\alpha - \alpha_{ss})] (1 - \xi) \sin 2\alpha]_{static} \\
&\quad + \text{Sgn}(\alpha') \pi R \cos \alpha \sin \alpha \quad \alpha_{ss} < \alpha < \alpha_{DM} \quad (31b)
\end{aligned}$$

FULLY SEPARATED FLOW THEORY

The dynamic drag in a fully separated flow is expressed by

$$C_D = \frac{2\pi \sin \alpha}{4 + \pi \sin \alpha} \left(1 + \sigma + \frac{\sigma^2}{8(\pi + 4)} \right) \sin \alpha + \text{Sgn}(\alpha') \pi R \cos \alpha \sin \alpha \quad \alpha > \alpha_{DM} \quad (32)$$

DYNAMIC DRAG : THEORY VS EXPERIMENT

FRANCIS AND KEESEE EXPERIMENTAL DATA

Again, the experimental data taken by Francis and Keesee [18] will now be used to evaluate the theory. Fig. 12 shows the change of foil angle with time and the corresponding response of dynamic drag coefficients at three frequencies of $R = 0.047$, 0.089 , and 0.130 . For the purpose of discussions, the enlarged dynamic drag curves are given in Fig. 19. The measured dynamic drag are given in Table 3 and plotted in Fig. 20. Aside from some scattering, the test data show a clear trend that the dynamic drag increases with the pitch rate.

NUMERICAL AND EXPERIMENTAL COMPARISON

Fully Attached Flow

Equation 31 is based on a two-dimensional theory. However, the model tested by Francis and Keesee is three-dimensional with an aspect ratio of 2.3. The induced drag must be incorporated in this comparison and is estimated by

$$(C_D)_{ind} = C_L^2 / \pi AR \quad (33)$$

The computed dynamic drag from Eq. 31 and 33 is given in Table 3 and plotted in Fig. 20. The good agreement between computations and measurements is very encouraging. However, it is noted that the induced drag is very large. Since the present model is based on a two-dimensional theory, two-dimensional test data, when available, must be used to further validate the numerical model. Any uncertainty produced by the three-dimensional effect in numerical evaluation must be removed.

Fully Separated Flow

The numerical results computed from Eq. 32 are given in Table 4 and plotted in Fig. 19 for $\alpha = 0.5, 0.6$ and 0.8 rad. In contrast to the fully attached flow case, the induced drag is seen to be relatively small when compared with the steady state form drag. The trend of drag vs angle is well predicted but the overall agreement between measurements and calculations is only fair. More test data are needed to validate the numerical model, especially from the two-dimensional unsteady test data.

UNSTEADY FLOW THEORIES FOR DYNAMIC PITCH MOMENT

Again, the Theodorsen solution [11] on a sinusoidal pitching and heaving motion is considered. The dynamic pitch moment M is given by

$$\begin{aligned} M = & \pi \rho b^2 [bah'' - b^2(1/8 + b^2) \alpha'] - \pi \rho b^3 U(1/2 - a) \alpha' \\ & + 2\pi \rho U b^2 (a + 1/2) C(K) [h' + U\alpha + b(1/2 - a) \alpha'] \end{aligned} \quad (34)$$

The α' term is known to be circulatory, but the coefficient is a constant and independent of reduced frequency K . As in the lift study, the α' term can be treated in the non-circulatory solution.

Let C_m , C_{mC} and C_{mNC} denote dynamic pitch moment coefficient, circulatory and non-circulatory moment coefficient, respectively. The moment is expressed by

$$C_m = C_{mC} + C_{mNC} \quad (35)$$

If h'' and α'' in Eq. 34 are not considered, the non-circulatory term is given by

$$C_{mNC} = -0.5\pi [(0.5 - a)] R \quad (36)$$

The Theodorsen solution on a sinusoidal pitching and heaving motion shows that the circulatory lift acts at the quarter chord. From a thin wing theory it is known that the steady lift also acts at the quarter chord. It is therefore assumed that the circulatory moment can be replaced by the steady moment. The dynamic pitch moment coefficient is given by

$$C_m = (C_m)_{steady} - 0.5\pi[(0.5 - a)]R \quad (37)$$

In the application for the PFM code, it is assumed that the resultant force acts at the quarter chord. The rotation axis is at the quarter chord on a propeller blade section. The coordinate system used in Theodorsen solution gives $a = -0.5$ and Eq. 37 is reduced to

$$C_m = (C_m)_{steady} - 0.5\pi R \quad \text{for } a = -0.5 \quad (38)$$

DYNAMIC MOMENT : THEORY VS EXPERIMENT

FRANCIS AND KEESEE EXPERIMENTAL DATA

Again, the experimental data taken by Francis and Keesee are used to evaluate the theory. Fig. 9 shows the change of foil angle with time and the corresponding response of moment coefficients at three frequencies of $R = 0.047, 0.089$, and 0.130 . For the purpose of discussions, the enlarged dynamic moment curves are given in Fig. 22.

As pointed out previously, stall is delayed by the unsteady motion. The lift increases almost linearly with the foil angle up to a certain critical angle termed the dynamic moment stall angle, α_{DM} , which is greater than the static stall angle, α_{ss} . Once the foil angle reaches the moment stall angle, the stall vortex starts to detach from the leading edge, with the resultant force moving rearward toward the trailing edge. The moment coefficient takes a divergence from the curve prior to the moment stall.

Fig. 22 shows that the moment curve vs angle of attack fluctuates along a mean line of $C_m = -0.13$ between $\alpha = 0.05$ to 0.55 rad for the test case of $R = 0.13$. At the foil angle greater than 0.55 rad, the moment curve starts to diverge from $C_m = -0.13$. Similarly, the lift curve given in Fig. 14c shows that the linear relationship between lift and foil angle breaks at $\alpha \approx 0.55$ rad. As expected a good correlation between lift and moment characteristics is observed.

At the pitch rate of $R = 0.089$, the moment curve fluctuates along a mean line of $C_m = -0.09$ between $\alpha = 0.02$ to 0.50 rad. The moment coefficient takes a divergence at 0.5 rad. The same characteristics also show up in the lift curve of Fig. 14b. At the pitch rate of $R = 0.047$, the moment curve fluctuates along a constant line of $C_m = -0.07$ between $\alpha = 0.02$ to 0.20 rad, and $C_m = -0.045$ between $\alpha = 0.20$ to 0.42 rad with an average of $C_m = -0.058$ between $\alpha = 0.02$ to 0.42 rad.

Experimental data further show that the moment curve after divergence is much steeper at a low pitch rate than at a high pitch rate. The lift data given in Fig. 14 also show this same trend that after the flow separated from the foil surface, the drop of lift with foil angle is much steeper at a low pitch rate than at a high pitch rate. This result shows a consistent trend between both lift and moment data. Pitch moment data show that the moment stall angles occur at $\alpha = 0.42, 0.50$ and 0.55 rad for pitch rates of $R = 0.047, 0.089$ and 0.130 respectively.

Results discussed so far can be summarized as follows. Measurements give $C_m = -0.058, -0.09$, and -0.13 for the pitch rates of $R = 0.047, 0.089$, and 0.130 , respectively. A significant effect on pitch moment coefficients due to unsteady motion is observed. These results will be compared with the computations.

Since steady moment data are not given by Francis and Keesee [18], test data given by Abbott and von Doenhoff [7] are shown in Fig. 22. The moment stall angle occurs at 13.7 deg (0.24 rad). At the foil angle less than 0.24 rad, the moment coefficient is around 0. Again, when compared with the dynamic data, the significant effect on pitch moment coefficients due to unsteady motion is clearly demonstrated.

NUMERICAL AND EXPERIMENTAL COMPARISON

First, Eq. 26 will be used to compute the moment stall angle. Recall that $\alpha_{ss} = 0.24$ rad (13.7 deg). The computed dynamic moment stall angles are $\alpha_{DM} = 0.43, 0.47$, and 0.51 rad for $R = 0.047, 0.089$, and 0.130 respectively. A good agreement between measurements and calculations is observed. This result is not surprising because the empirical formula given in Eq. 26 is derived from Francis and Keesee test data.

Next the dynamic moment coefficients are computed from Eq. 38. Recall that Francis and Keesee tests were conducted with the foil rotated along the axis at 31.7% from the leading edge. This axis gives a $a = -0.336$ in Theodorsen's coordinate system. The computed and measured moment coefficients at angles less than α_{DM} are given in Table 5 along with the stall angles. Note that the negative sign on moment coefficient denote a nose down pitch moment.

The pitch down moment is over-predicted by the theory especially at high pitch rates. However, the trend due to unsteady effect is correctly predicted.

CONCLUSIONS

Significant dynamic effects on propeller blade section lift, drag, and pitching moment coefficients are observed in this study. The variation in inflow angle during maneuvers can be reasonably approximated by ramp-up and ramp-down motions. Based on classic aerodynamic theory with ramp-up ramp-down motions, the dynamic lift, drag and pitching moment are expressed by circulatory and non-circulatory flow solutions.

The dynamic theories are compared with Francis and Keesee experimental data. The computed dynamic lift is shown to be substantially greater than the static lift especially at angles

greater than the static stall angle. The computed dynamic lift is seen to under-predict the measurements. However, if the term related to Wagner's function is not considered, the computed and measure dynamic lift agrees very well with all three reduced frequencies compared. Further studies are needed to examine the effects of Wagner function.

The good correlation obtained between computed and measured dynamic drag is very encouraging. The relationship between pitching moment and reduced frequencies is reasonably predicted but the theory over-predicts the change of pitching moment coefficients due to an unsteady motion.

Many assumptions have been introduced in developing the present dynamic models. More test data especially two-dimensional dynamic data are needed to validate the present dynamic models.

ACKNOWLEDGMENTS

The authors would like to thank Carol Tseng and Janet Andrews for their help in the preparation of this report and to Gordon Leishman at the University of Maryland for his technical advice.

THIS PAGE IS INTENTIONALLY LEFT BLANK

Table 1. Dynamic vs static lift slope.

<u>Airfoil</u>	<u>Static Lift Slope</u>	<u>Dynamic Lift Slope</u>
NACA 0012	0.109	0.101
Ames-01	0.112	0.105
Wortman FX-098	0.109	0.103
Sikorsky SC-1095	0.118	0.110
Hughes HH-02	0.114	0.108
Vertol VR-7	0.117	0.104
NRL-1	0.103	0.102

Table 2. Computed and Measured Dynamic Lift.(a) $\alpha = 0.1$ rad $(C_L)_{\text{static}} = 0.40$ at $\alpha = 0.1$ rad, $\partial C_L / \partial \alpha = 3.4$

R	t sec	α_w Eq. 19	$(\partial C_L / \partial \alpha) \alpha_w$ x 0.94	πR	Computed C_L Eq. 22a	Computed C_L Eq. 22a with $\alpha_w = 0$	Measured C_L Ref. [18]
0.047	0.032	0.034	0.109	0.148	0.439	0.548	0.61
0.089	0.026	0.036	0.115	0.280	0.565	0.680	0.67
0.130	0.024	0.037	0.118	0.408	0.690	0.808	0.86

(b) $\alpha = 0.2$ rad $(C_L)_{\text{static}} = 0.74$ at $\alpha = 0.2$ rad, $\partial C_L / \partial \alpha = 3.4$

R	t sec	α_w Eq. 19	$(\partial C_L / \partial \alpha) \alpha_w$ x 0.94	πR	Computed C_L Eq. 22a	Computed C_L Eq. 22a with $\alpha_w = 0$	Measured C_L Ref. [18]
0.047	0.046	0.060	0.192	0.148	0.696	0.888	0.90
0.089	0.035	0.066	0.211	0.280	0.809	1.020	1.01
0.130	0.031	0.069	0.220	0.408	0.928	1.148	1.21

(c) $\alpha = 0.3$ rad $(C_L)_{ss} = 0.88$ at $\alpha_{ss} = 0.242$ rad, $\partial C_L / \partial \alpha = 3.4$

R	t sec	α_w Eq. 19	$(\partial C_L / \partial \alpha) \alpha_w$ x 0.94	πR	Computed C_L Eq. (22b)	Computed C_L Eq. 22b with $\alpha_w = 0$	Measured C_L Ref. [18]
0.047	0.060	0.083	0.265	0.148	0.960	1.225	1.18
0.089	0.044	0.093	0.297	0.280	1.060	1.357	1.43
0.130	0.037	0.098	0.313	0.408	1.172	1.485	1.54

(d) $\alpha = 0.4$ rad $(C_L)_{ss} = 0.88$ at $\alpha_{ss} = 0.242$ rad, $\partial C_L / \partial \alpha = 3.4$

R	t sec	α_w Eq. 19	$(\partial C_L / \partial \alpha) \alpha_w$ x 0.94	πR	Computed C_L Eq. 22b	Computed C_L Eq. 22b with $\alpha_w = 0$	Measured C_L Ref. [18]
0.047	0.080	0.098	0.313	0.148	1.252	1.565	1.51
0.089	0.053	0.115	0.367	0.280	1.329	1.697	1.66
0.130	0.043	0.124	0.396	0.408	1.428	1.825	1.88

Table 3. Dynamic Drag in an Attached Flow.

$$C_{DF} = 0.0058, (C_L)_{ss} = 0.88 \text{ at } \alpha_{ss} = 0.242, \partial C_L / \partial \alpha = 3.4, \text{ and } \xi = 0.97$$

(a) Pitch Rate of $R = 0.047$

α	$(C_L)_{st}$	$(C_D)_{ind}$	$\pi R \cos \alpha \sin \alpha$	$0.5 (C_L)_{st} (1 - \xi) \sin 2\alpha]$	C_D
0.1	0.40	0.022	0.015	0.0012	0.044
0.2	0.74	0.076	0.029	0.0044	0.115
0.3	1.08	0.161	0.042	0.0091	0.218
0.4	1.42	0.278	0.053	0.0160	0.353

(b) Pitch Rate of $R = 0.089$

α	$(C_L)_{st}$	$(C_D)_{ind}$	$\pi R \cos \alpha \sin \alpha$	$0.5 (C_L)_{st} (1 - \xi) \sin 2\alpha]$	C_D
0.1	0.40	0.022	0.028	0.0012	0.057
0.2	0.74	0.076	0.054	0.0044	0.141
0.3	1.08	0.161	0.079	0.0091	0.255
0.4	1.42	0.278	0.1010	0.0160	0.400

(c) Pitch Rate of $R = 0.130$

α	$(C_L)_{st}$	$(C_D)_{ind}$	$\pi R \cos \alpha \sin \alpha$	$0.5 (C_L)_{st} (1 - \xi) \sin 2\alpha]$	C_D
0.1	0.40	0.022	0.041	0.0012	0.070
0.2	0.74	0.076	0.080	0.0044	0.166
0.3	1.08	0.161	0.115	0.0091	0.291
0.4	1.42	0.278	0.147	0.0160	0.447

Table 4. Computed Dynamic Drag in a Separated Flow.

(a) Pitch Rate $R = 0.047$

Angle (rad)	σ Fig. 2	C_L Eq. 3b	$(C_D)_{ind}$ Eq. 33	$(C_D)_{st}$ Eq. 6	$\pi R \cos \alpha \sin \alpha$	C_D Eq. 32
0.5	0.93	0.933	0.120	0.509	0.062	0.691
0.6	1.00	1.057	0.154	0.701	0.069	0.924
0.8	1.18	1.126	0.175	1.139	0.074	1.388

(b) Pitch Rate $R = 0.089$

Angle (rad)	σ Fig. 2	C_L Eq. 3b	$(C_D)_{ind}$ Eq. 33	$(C_D)_{st}$ Eq. 6	$\pi R \cos \alpha \sin \alpha$	C_D Eq. 32
0.5	0.93	0.933	0.120	0.509	0.118	0.747
0.6	1.00	1.057	0.154	0.701	0.130	0.985
0.8	1.18	1.126	0.175	1.139	0.140	1.454

(c) Pitch Rate $R = 0.130$

Angle (rad)	σ Fig. 2	C_L Eq. 3b	$(C_D)_{ind}$ Eq. 33	$(C_D)_{st}$ Eq. 6	$\pi R \cos \alpha \sin \alpha$	C_D Eq. 32
0.5	0.93	0.933	0.120	0.509	0.172	0.801
0.6	1.00	1.057	0.154	0.701	0.190	1.045
0.8	1.18	1.126	0.175	1.139	0.204	1.518

Table 5. Moment Stall Angles and Moment Coefficients.

Pitch Rate R	Computed		Measured	
	α_{DM} Eq. 26	C_m Eq. 37	α_{DM}	C_m
0			0.24	0
0.047	0.43	-0.064	0.42	-0.058
0.089	0.47	-0.121	0.50	-0.090
0.130	0.51	-0.177	0.55	-0.130

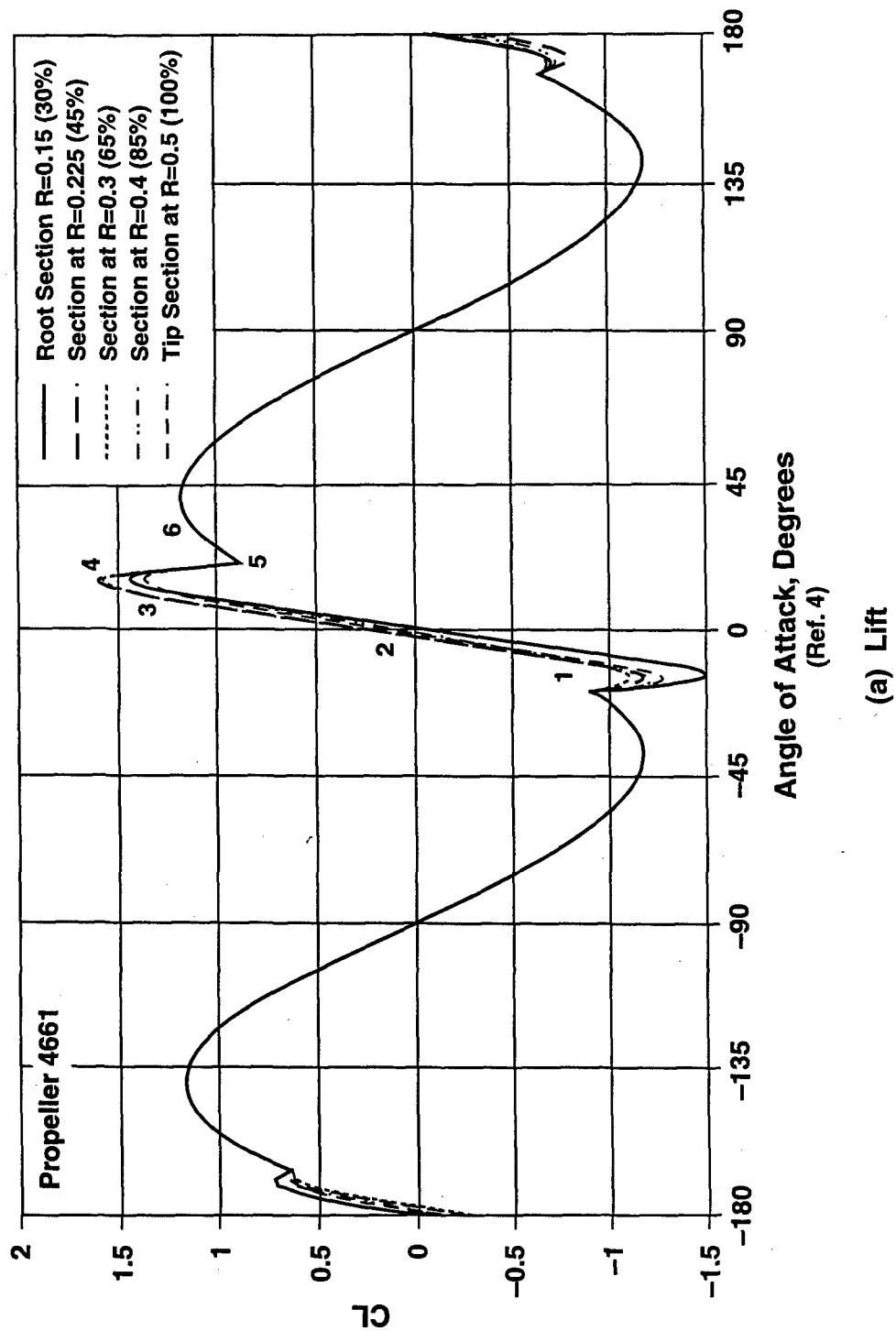


Fig. 1. Section lift, drag and pitch moment characteristics.

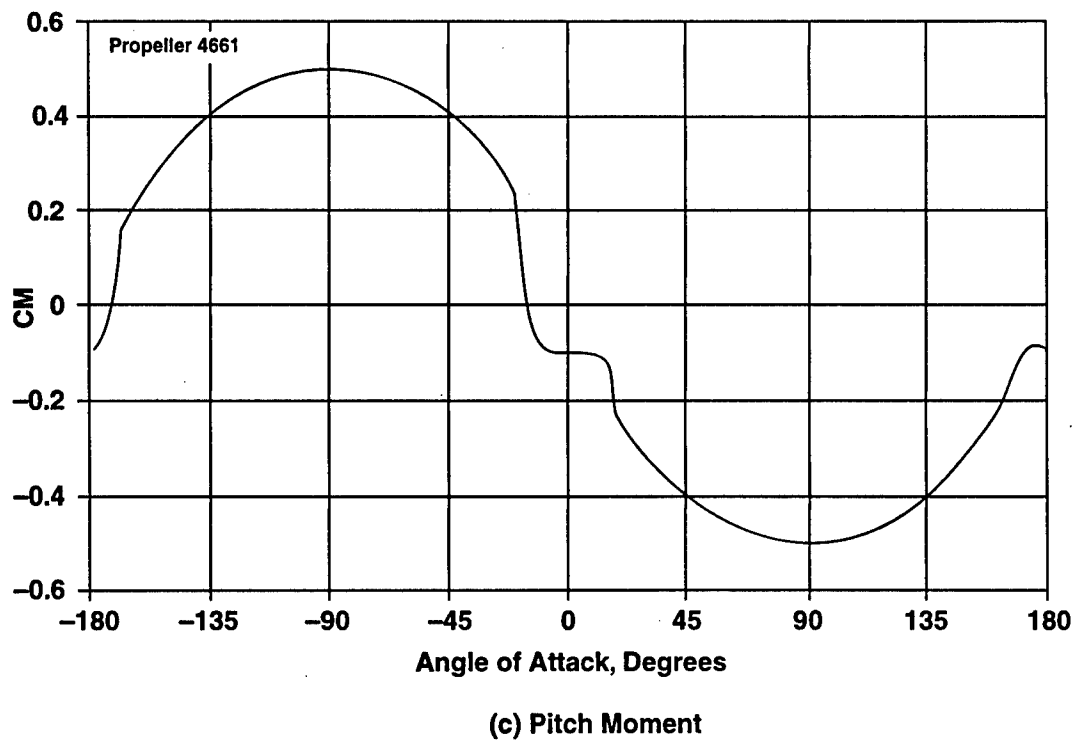
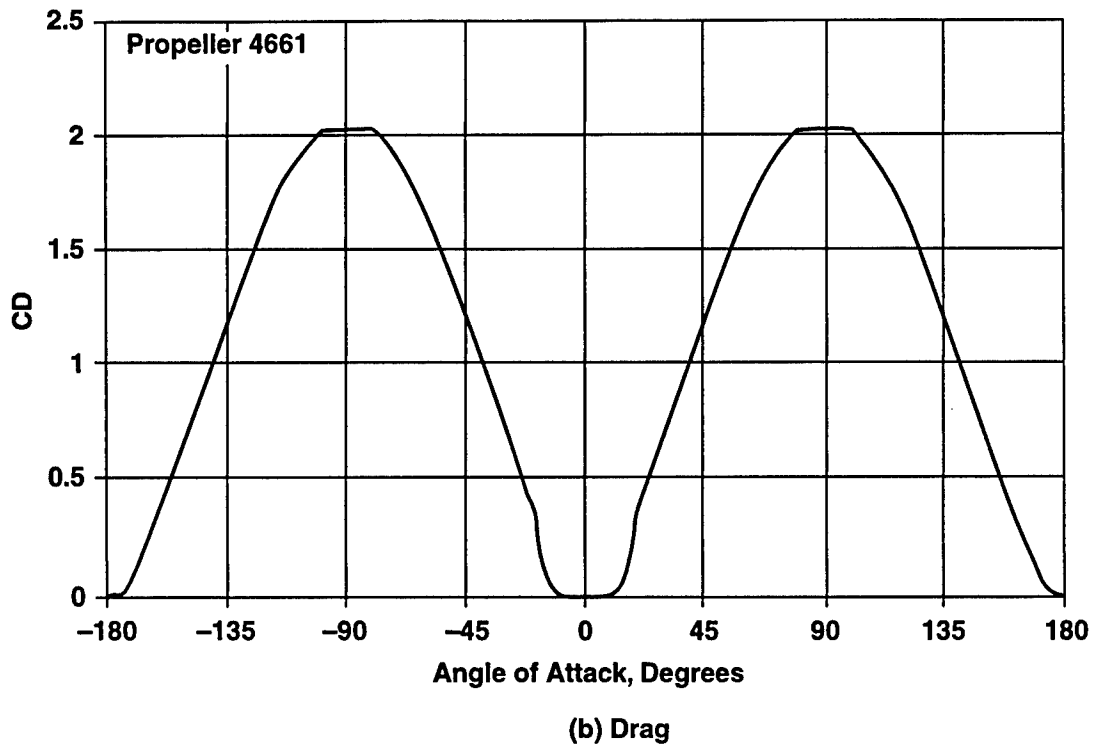


Figure 1. (Continued)

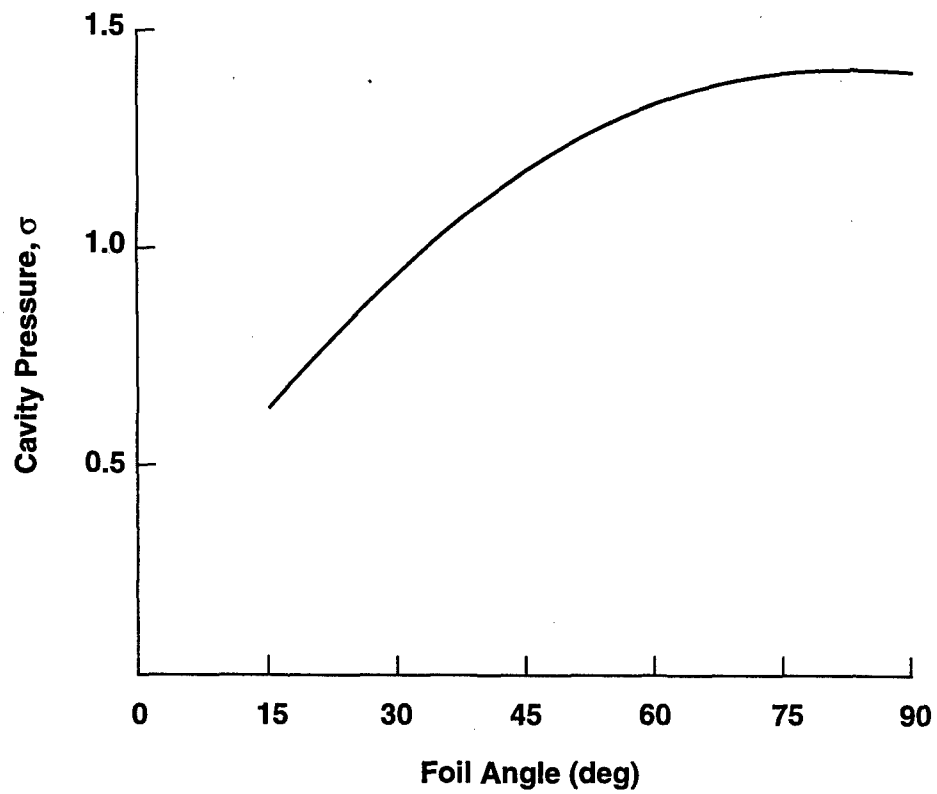


Figure 2. Pressure inside a separated flow cavity as a function of foil angle.

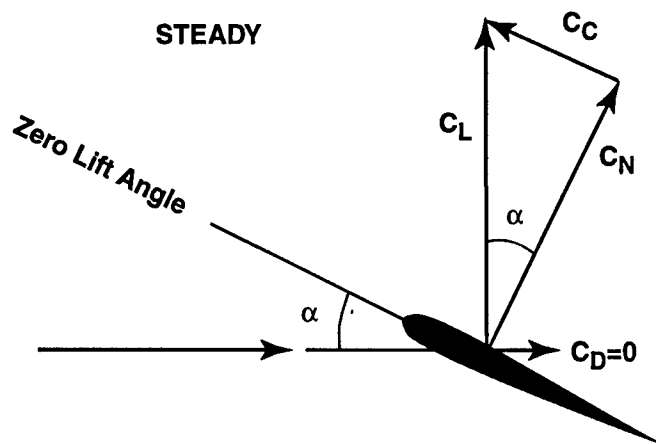


Fig. 3. Force resolution on an airfoil in unsteady flow.

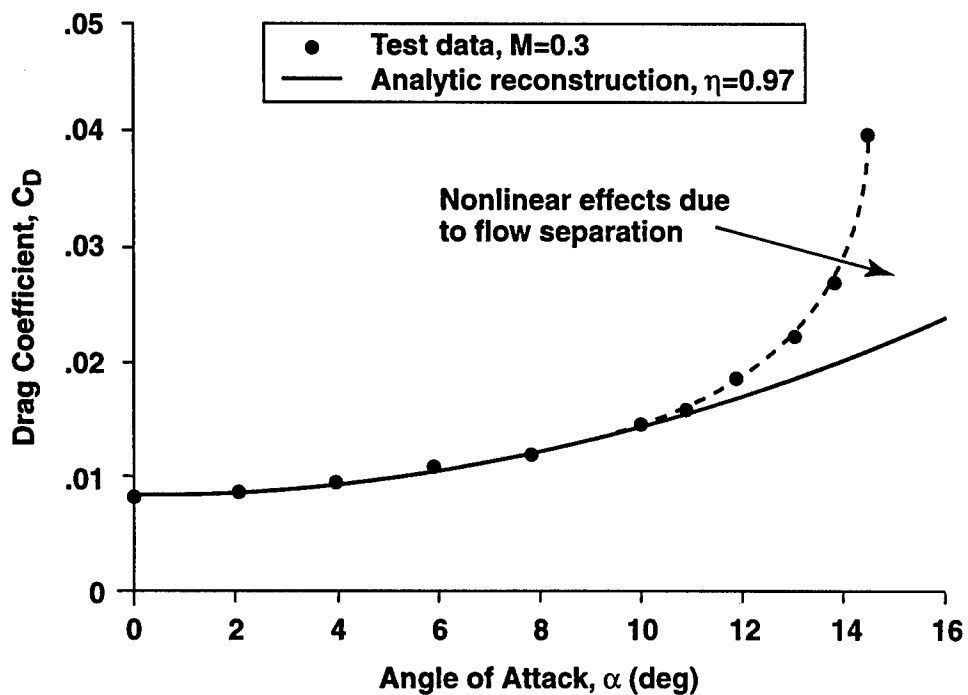
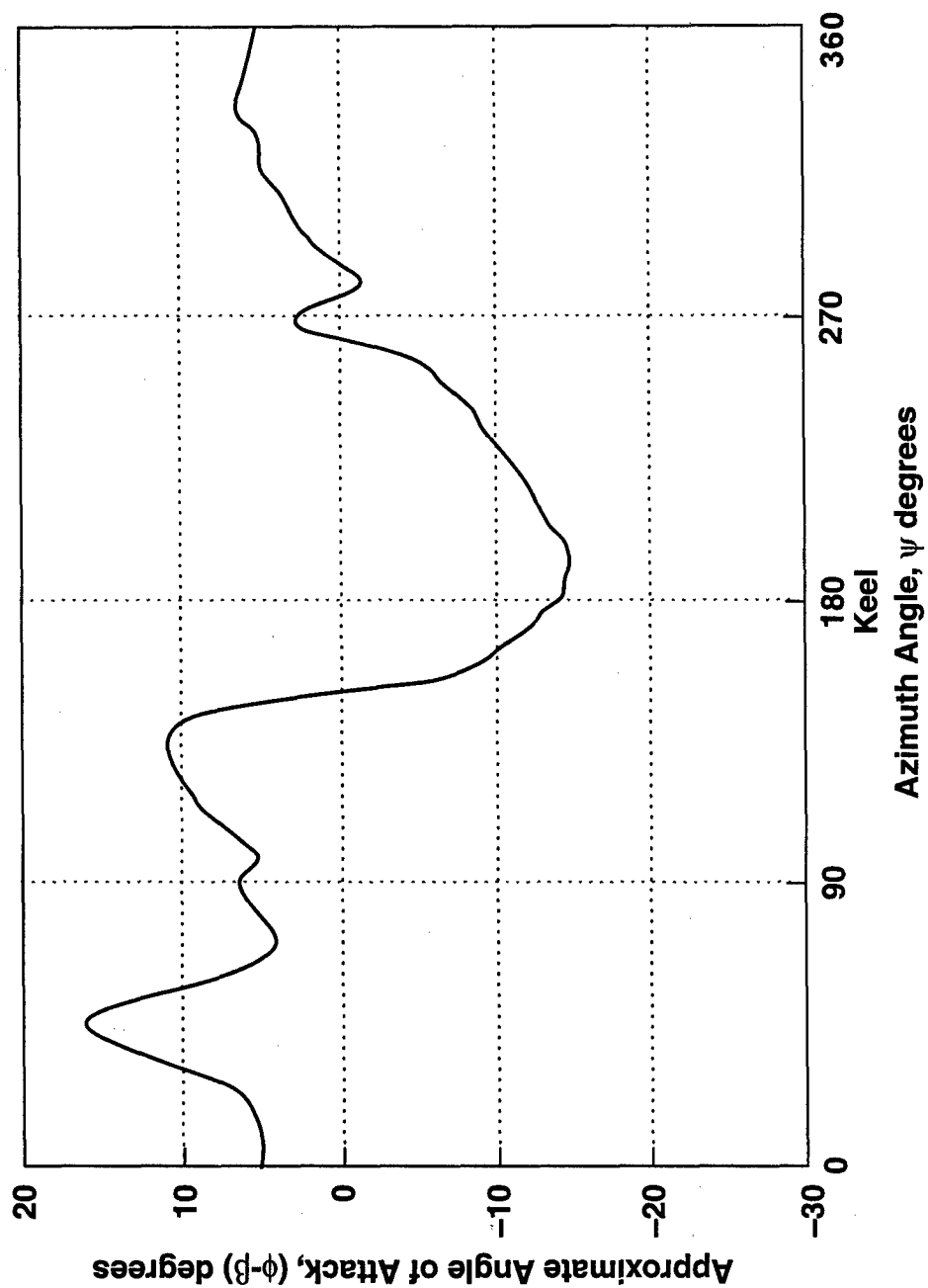
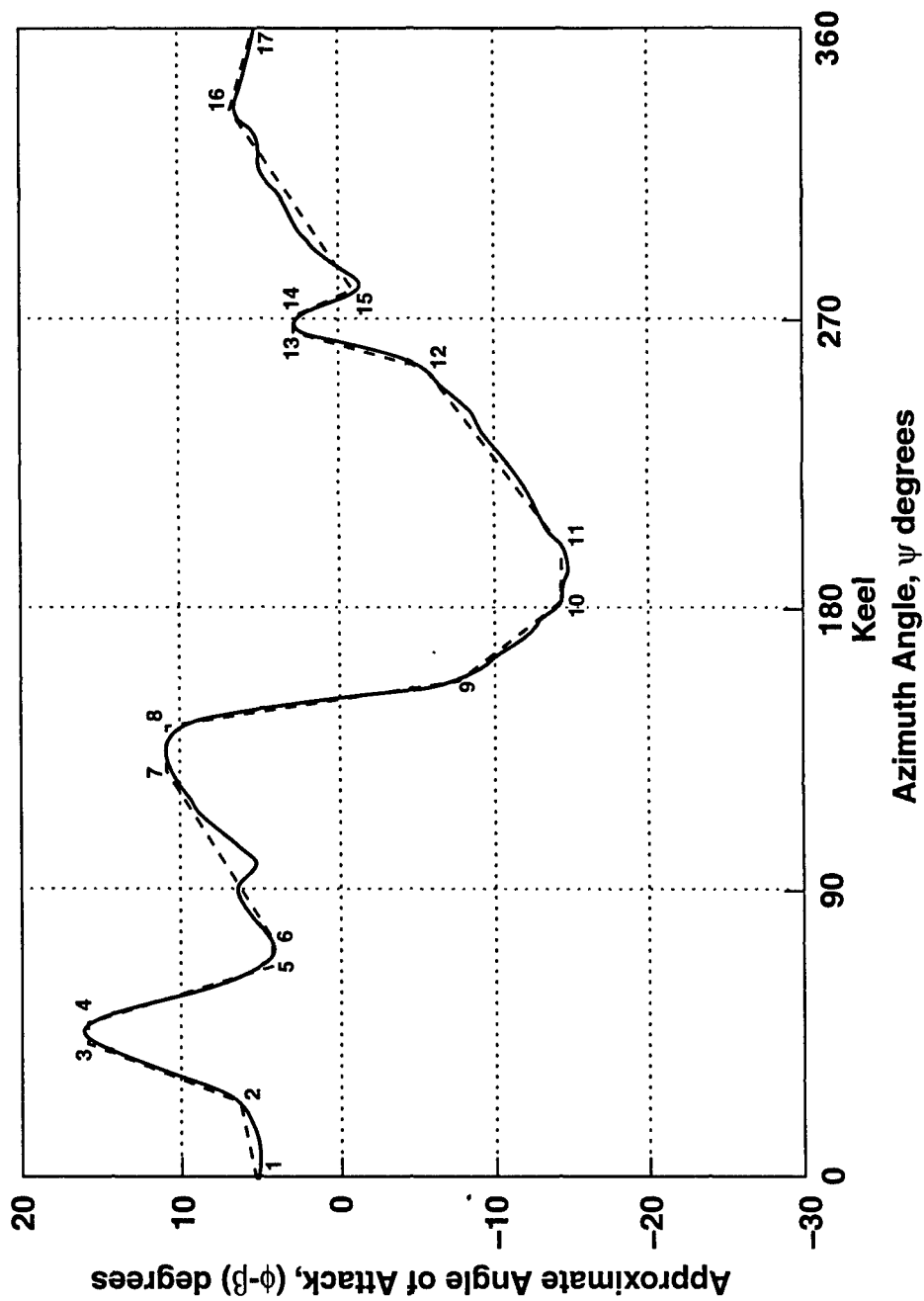


Fig. 4. Modeling of steady drag for nominally attached flow (Ref. 6).



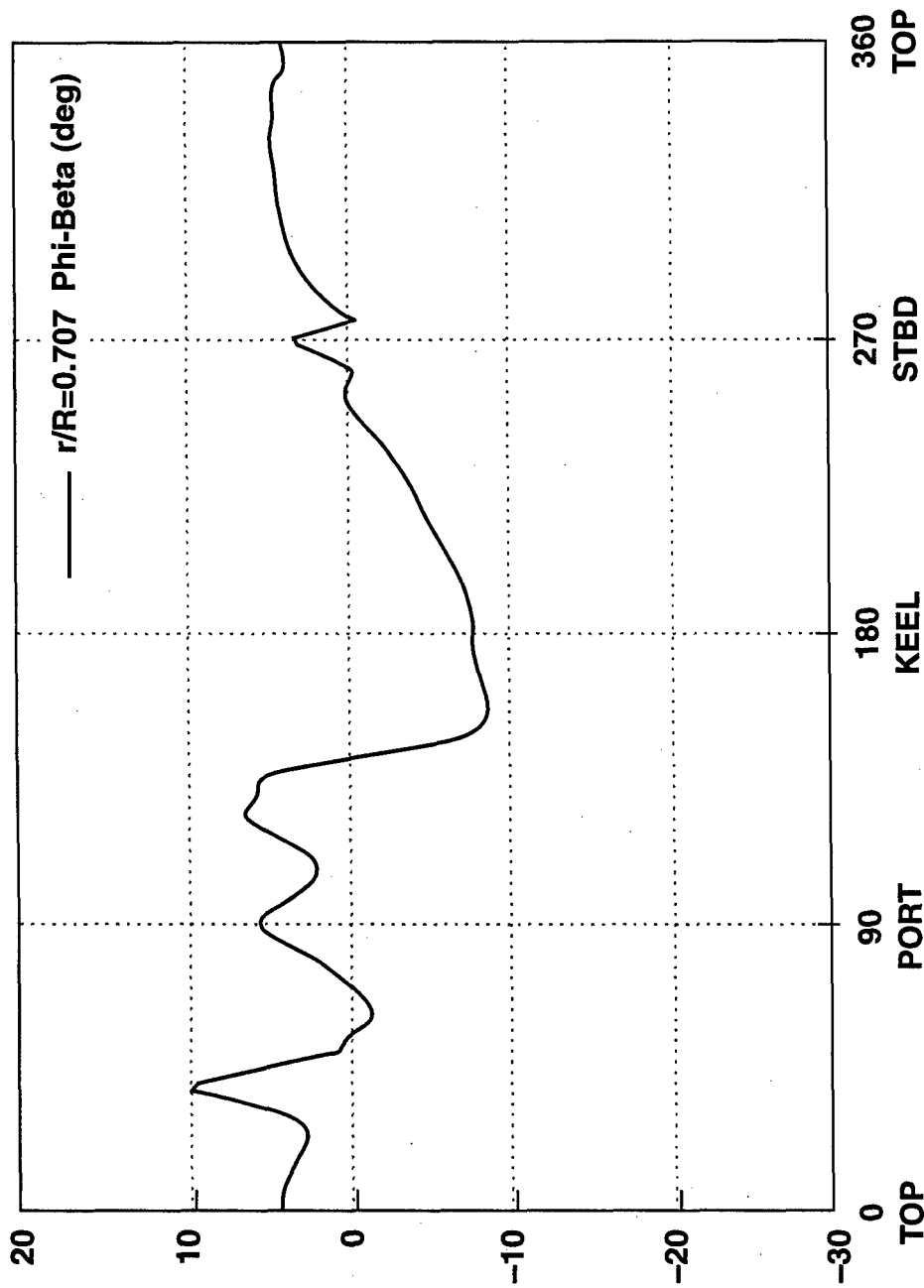
(a) Inflow angle

Fig. 5. Inflow angles in the propeller plane at $r/R=0.4$ for a typical turn.



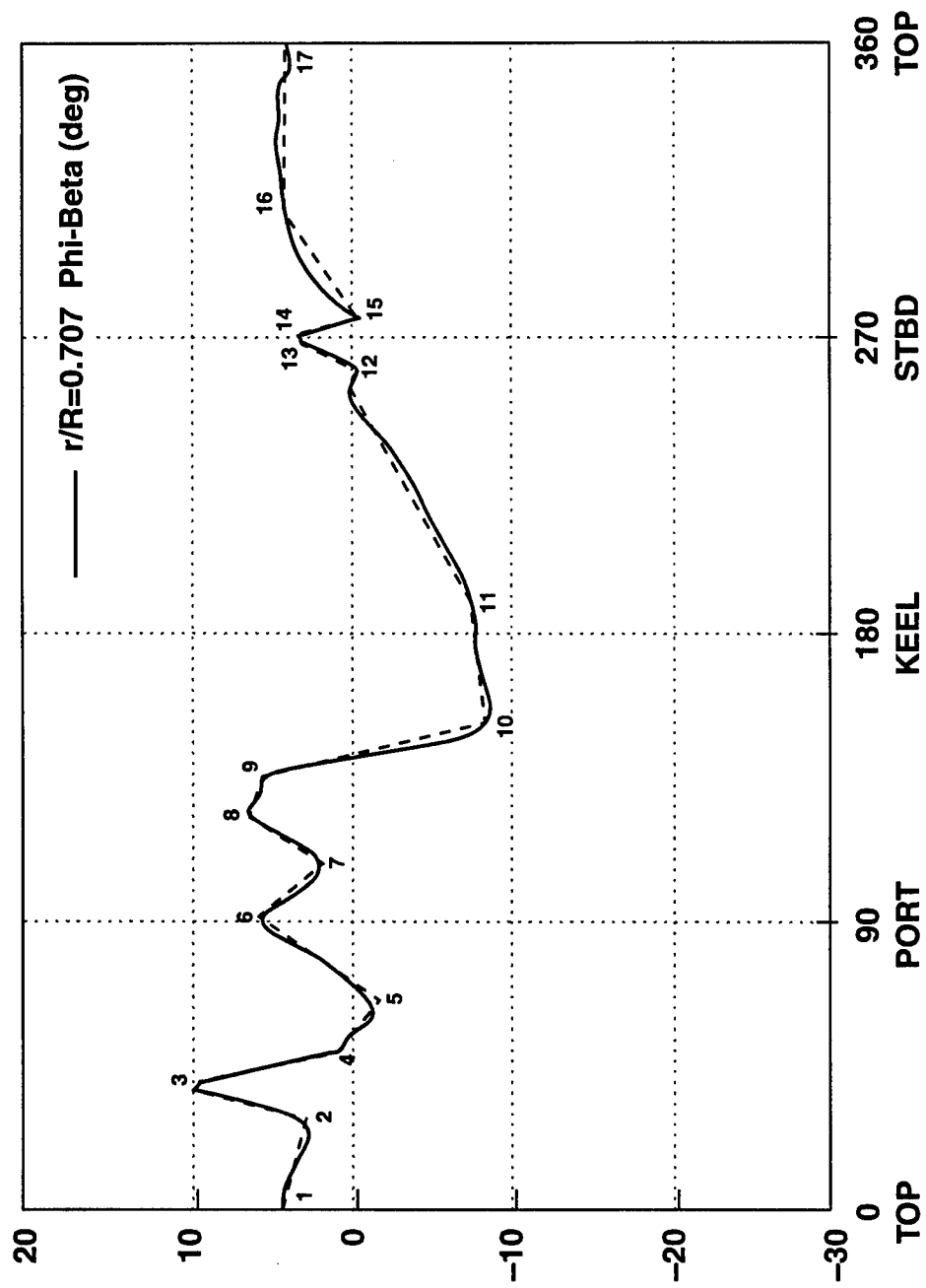
(b) Inflow angle segmented

Fig. 5. (Continued)



(a) Inflow angle

Fig. 6. Approximate angles of attack in left turn.



(b) Inflow angle segmented

Fig. 6. (Continued)

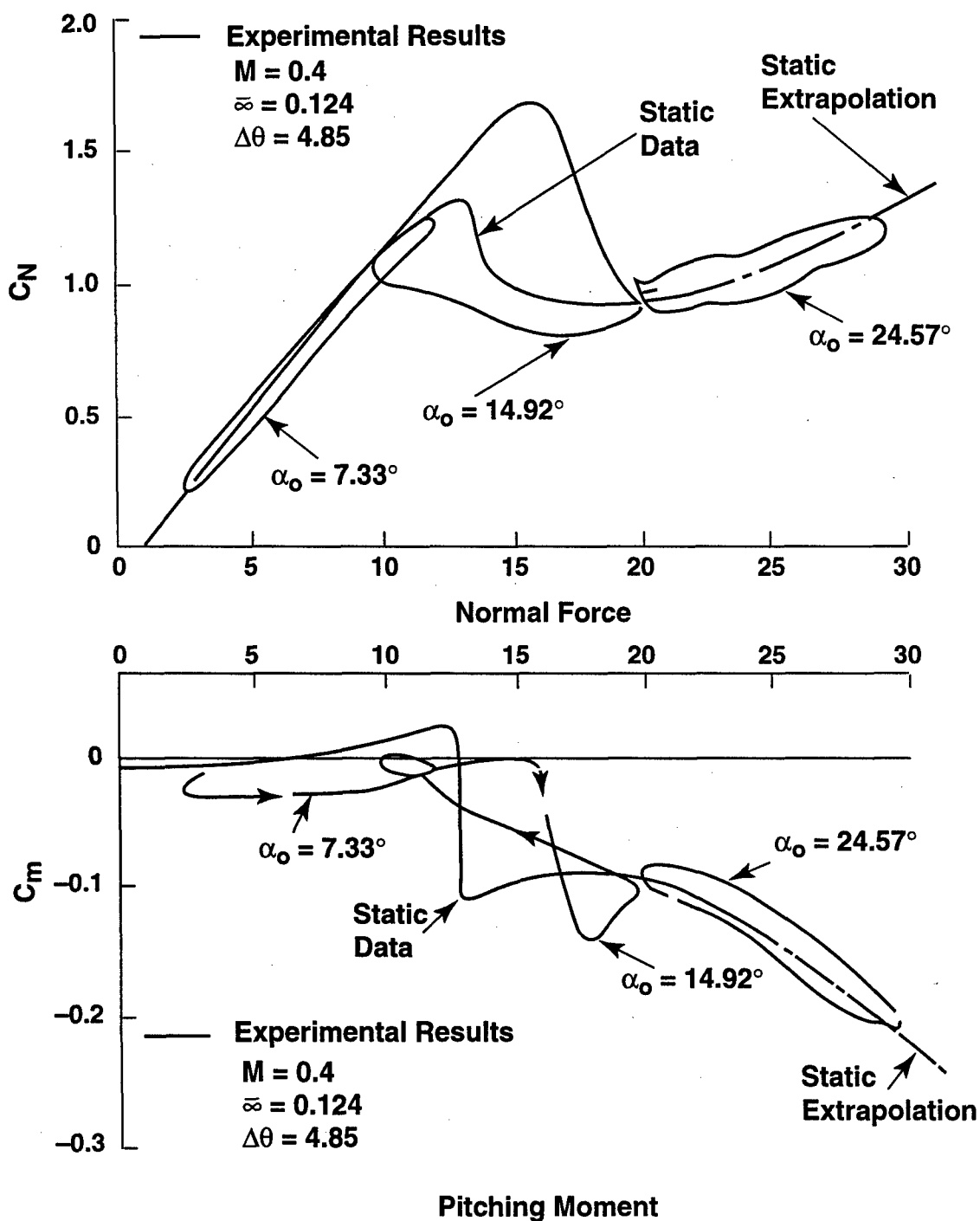


Fig 7. Effect of angle of attack on dynamic characteristics
 (Vertol 23010-1.58 Airfoil Section) (Ref. 9).

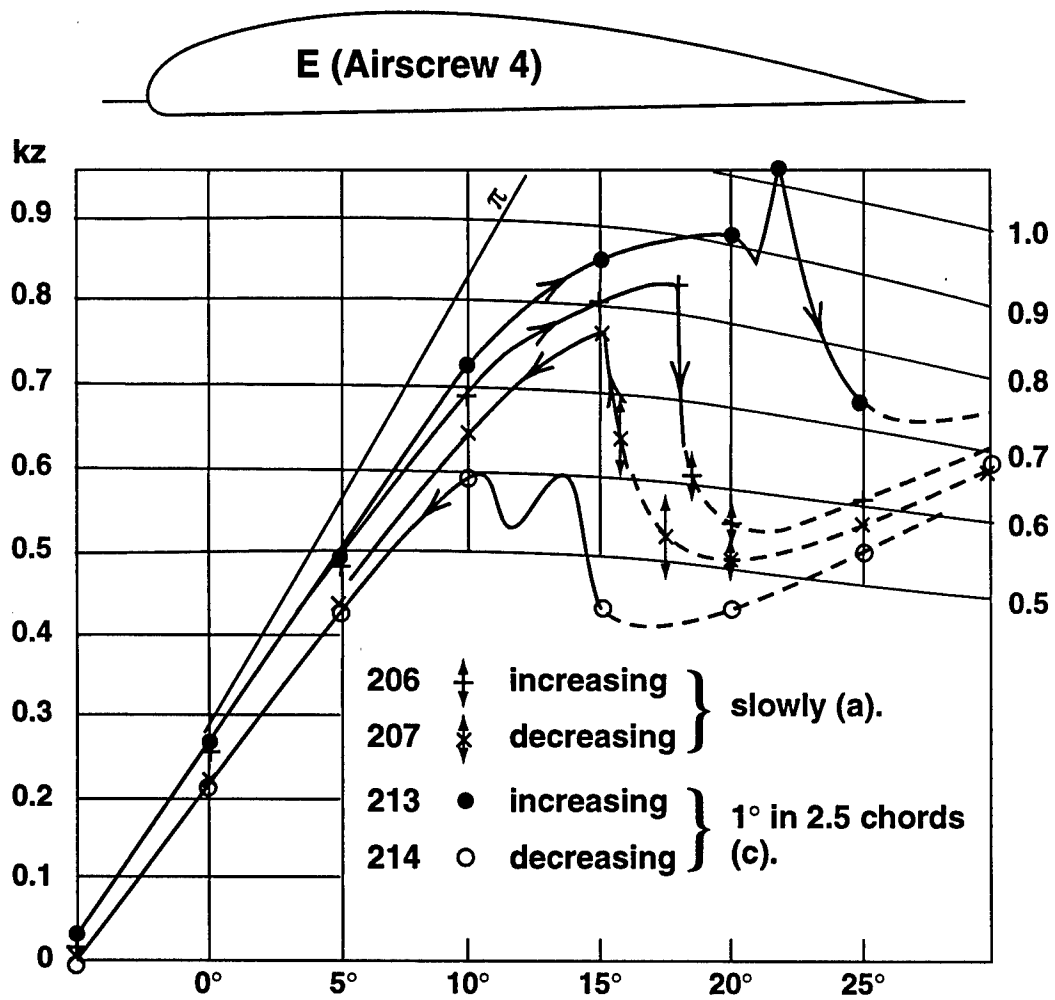


Fig. 8. Reduced records of normal and longitudinal force for Profile B (Ref. 10).

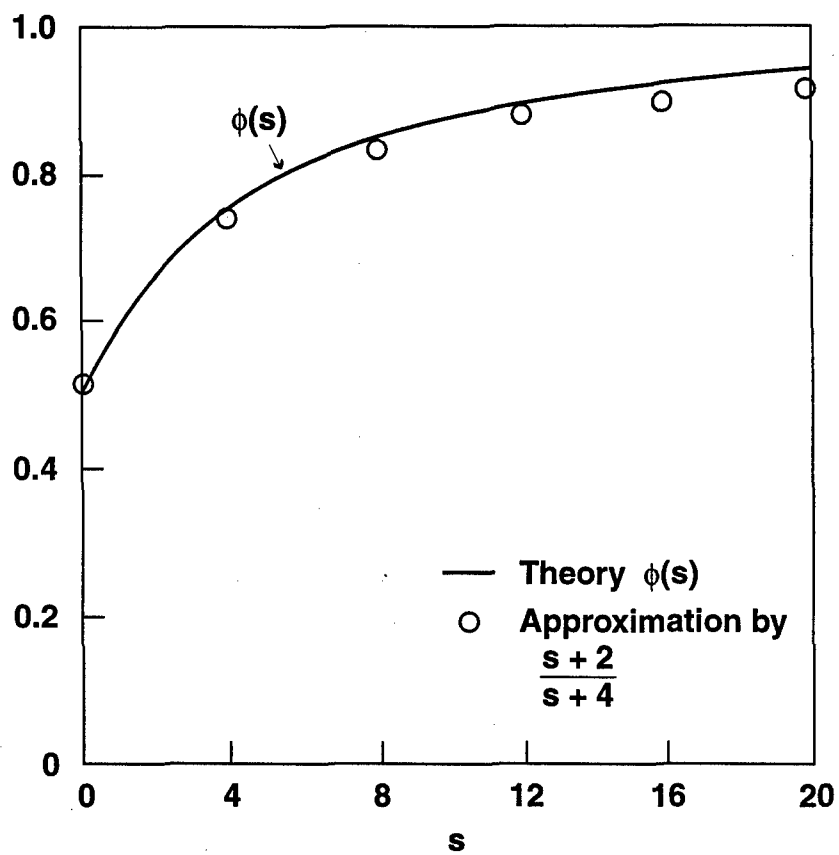


Fig. 9. Wagner function $\phi(s)$ and approximation.

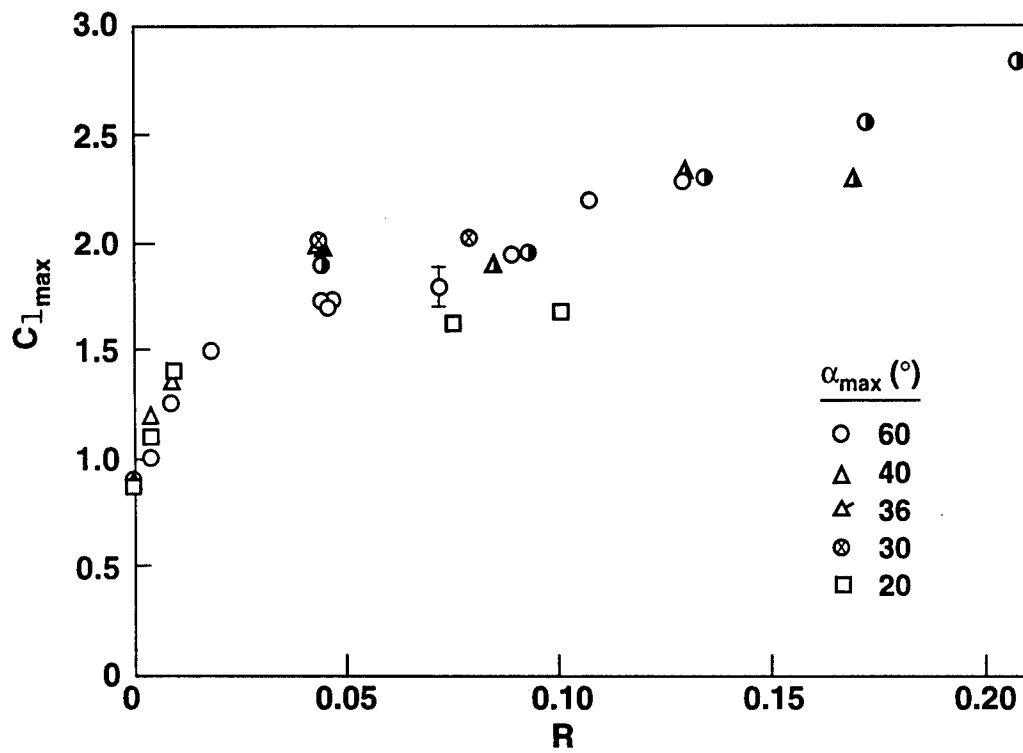


Fig. 10. Maximum lift coefficient variation with pitch rate (Ref. 18).
[open symbols—NACA 0012, half-solid symbols—NACA 641A012]

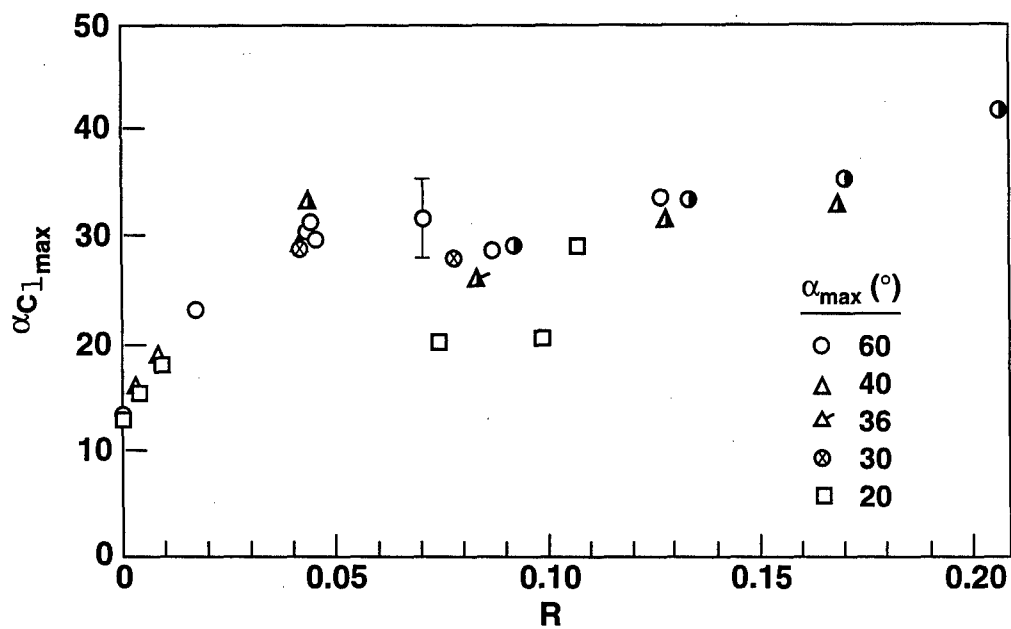


Fig. 11. Angle-of-attack for maximum lift coefficient variation with pitch rate (Ref. 18).
[open symbols—NACA 0012, half-solid symbols—NACA 641A012]

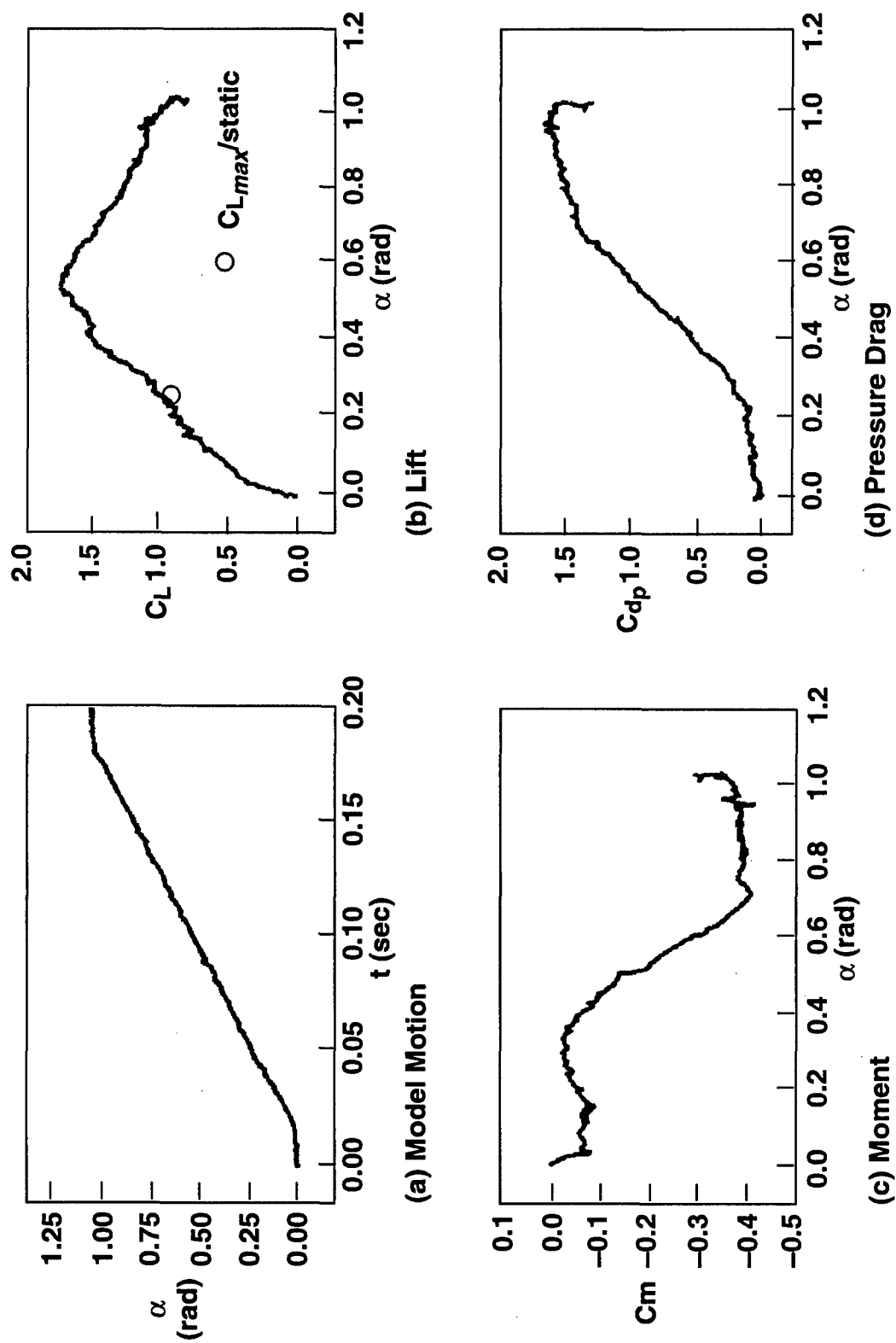
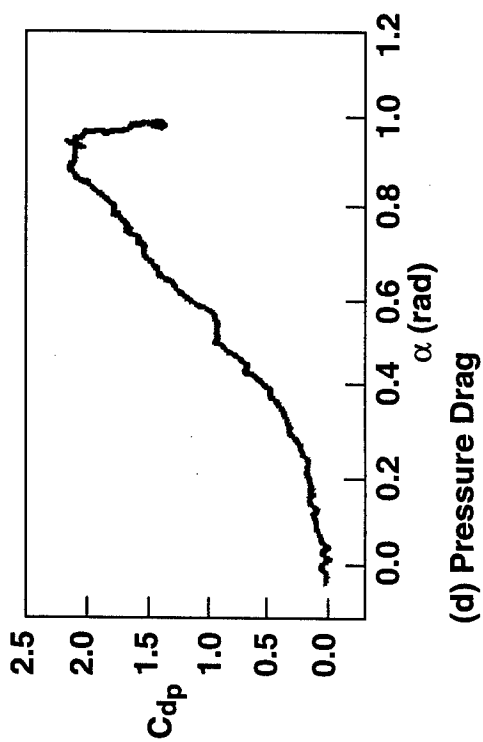
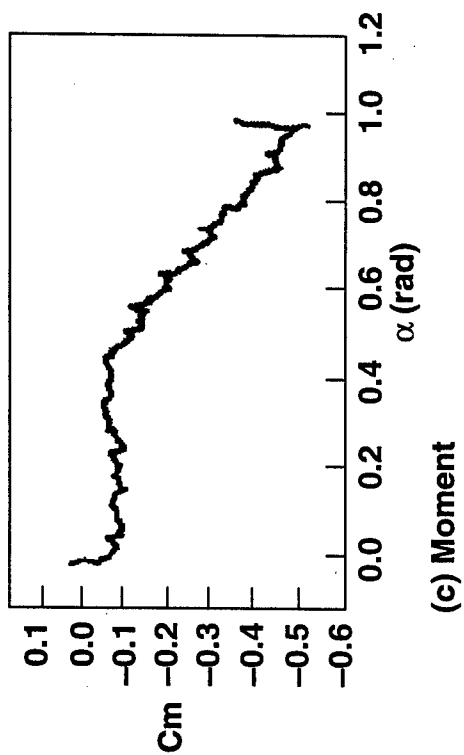
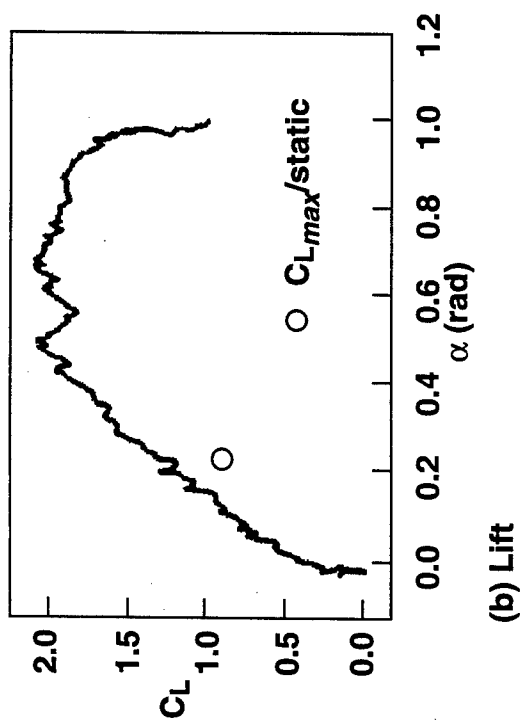
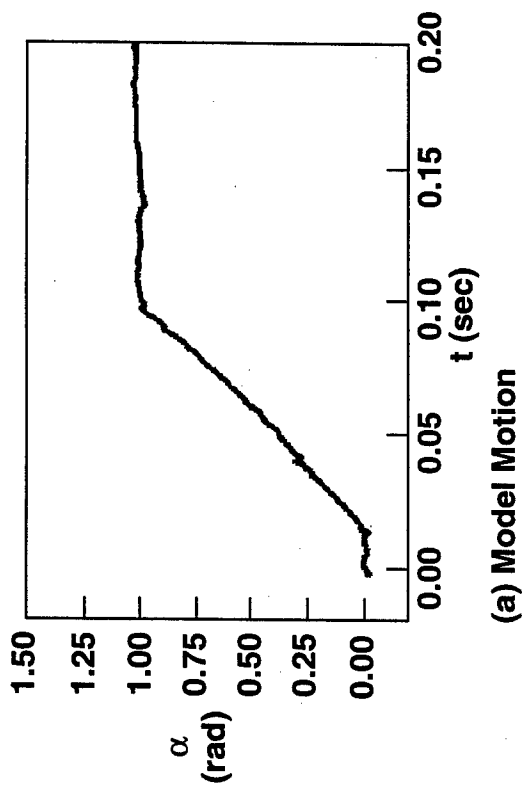
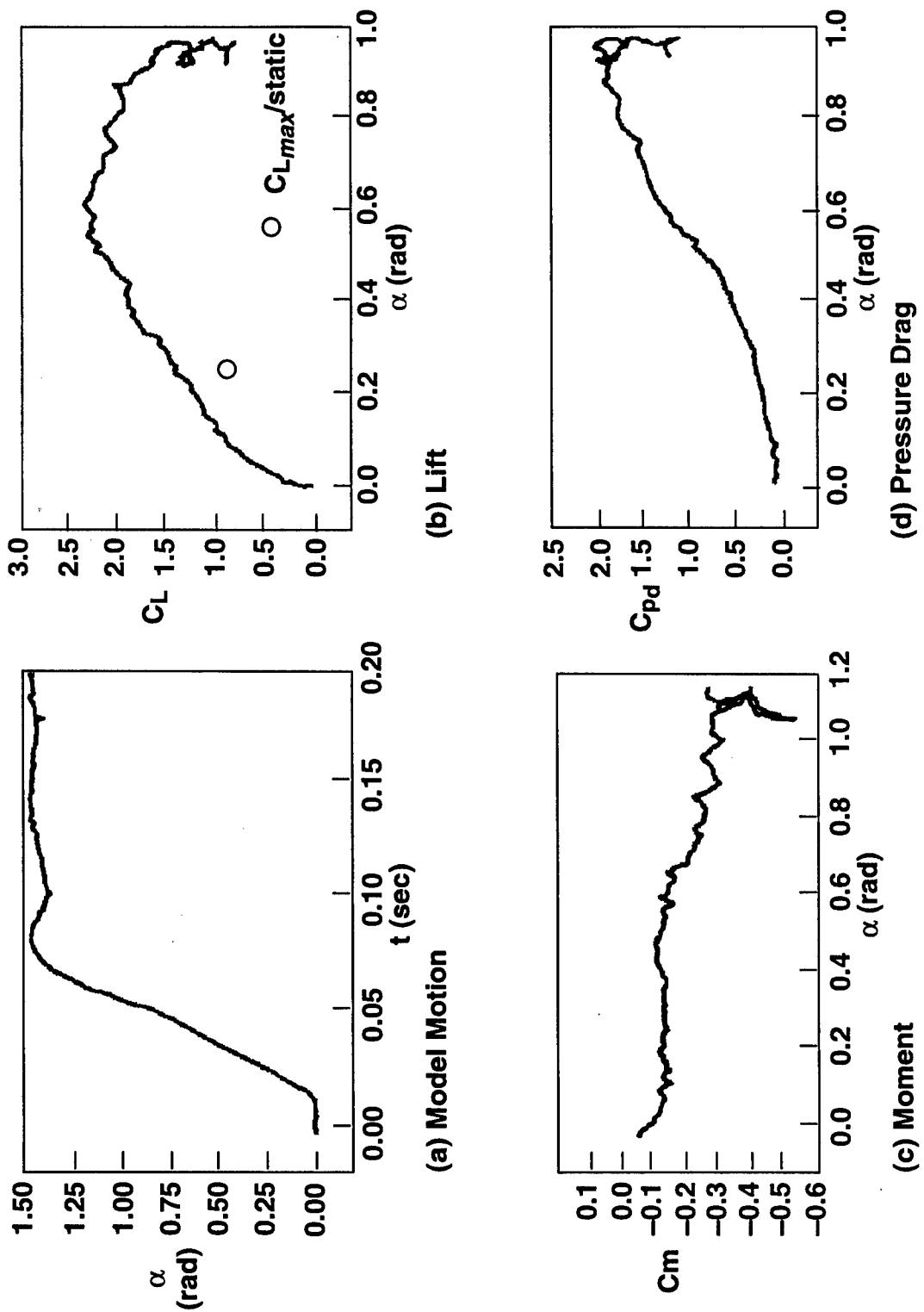


Fig. 12. Force and moment characteristics: NACA 0012, $U_{\infty} = 33.1$ ft.s (10.1 m/s).



(b) $R = 0.089$

Fig. 12. (Continued)



(c) $R=0.130$

Fig. 12. (Continued)

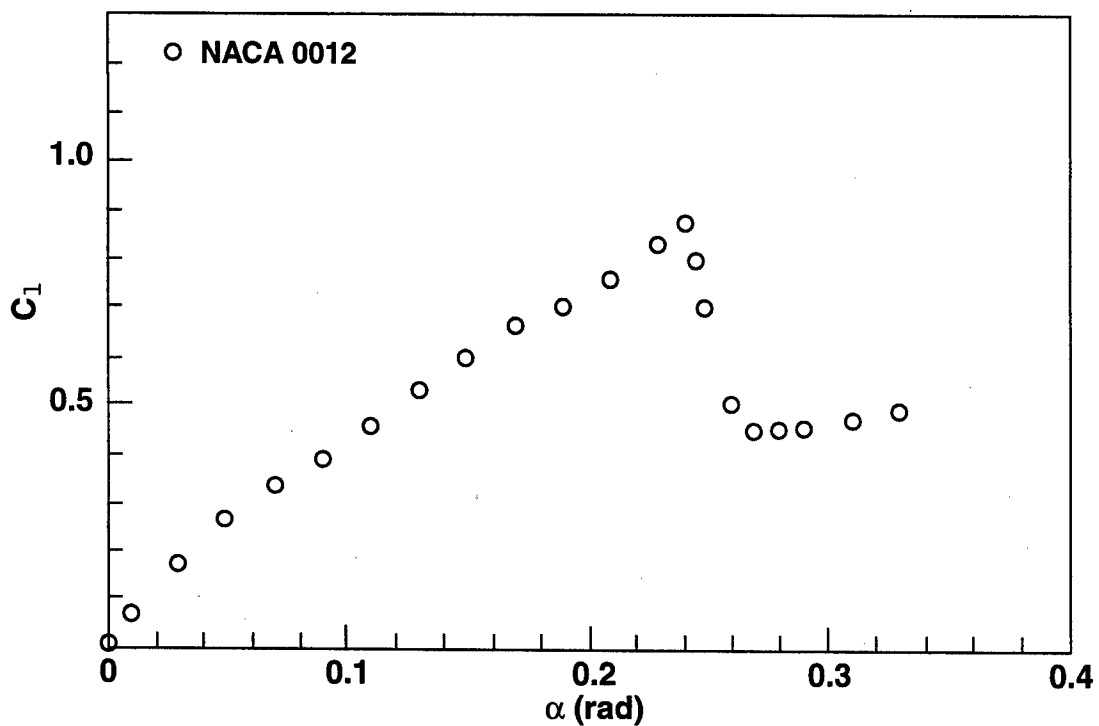


Fig. 13. Steady flow lift characteristics, $k=0$ (Ref. 18).

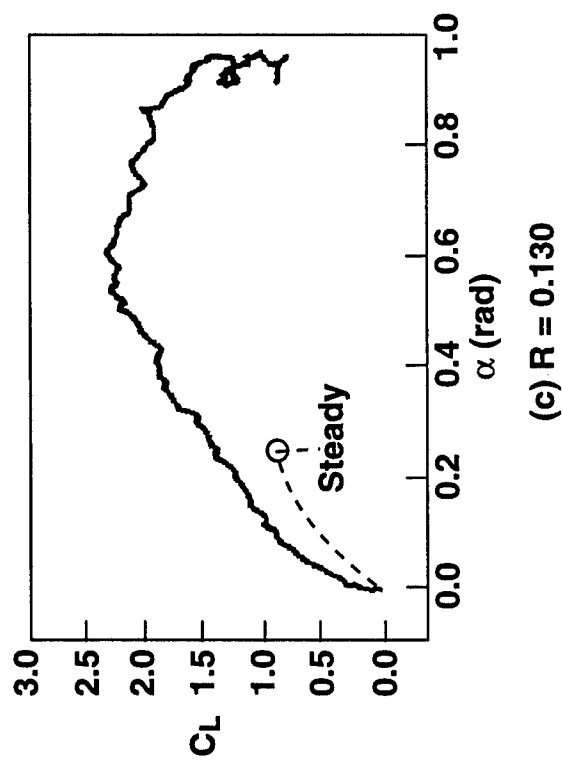
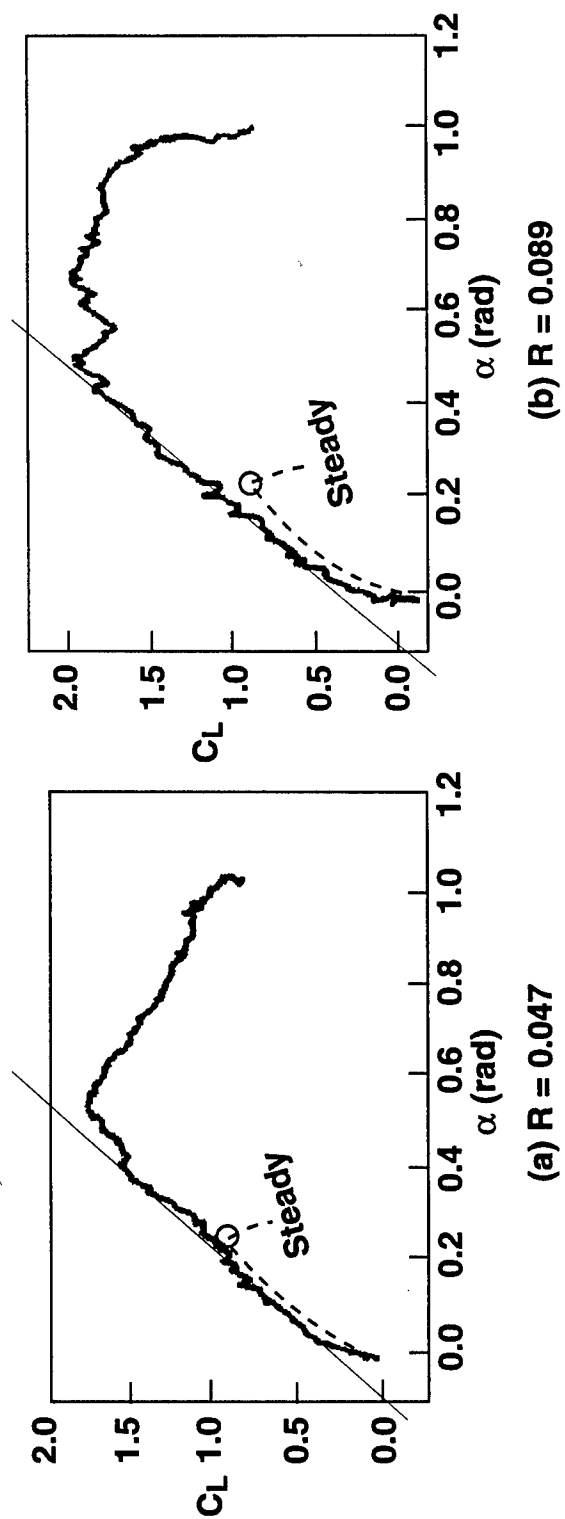


Fig. 14. Unsteady flow.

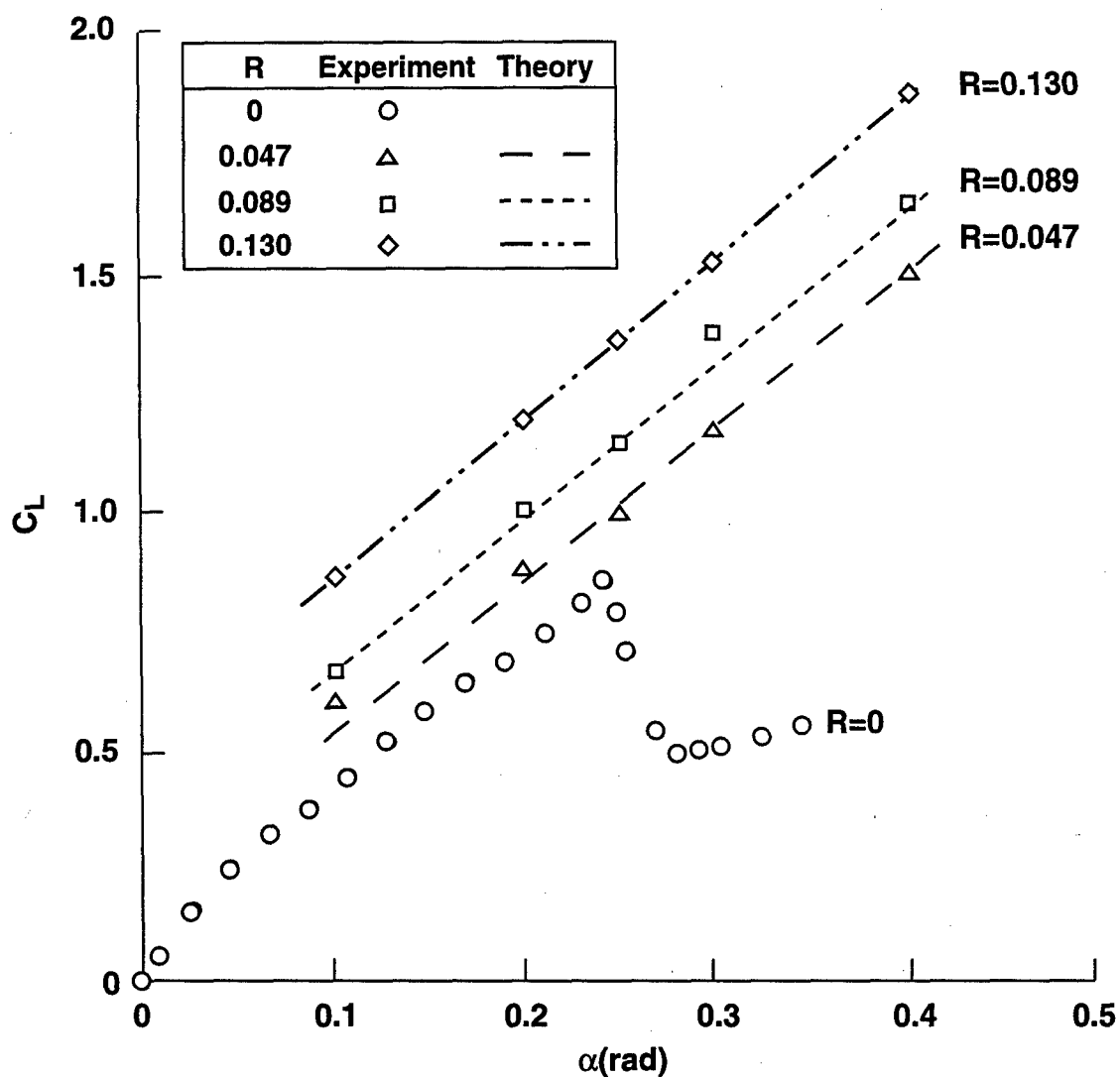


Fig. 15. Unsteady effects on lift: experiments.

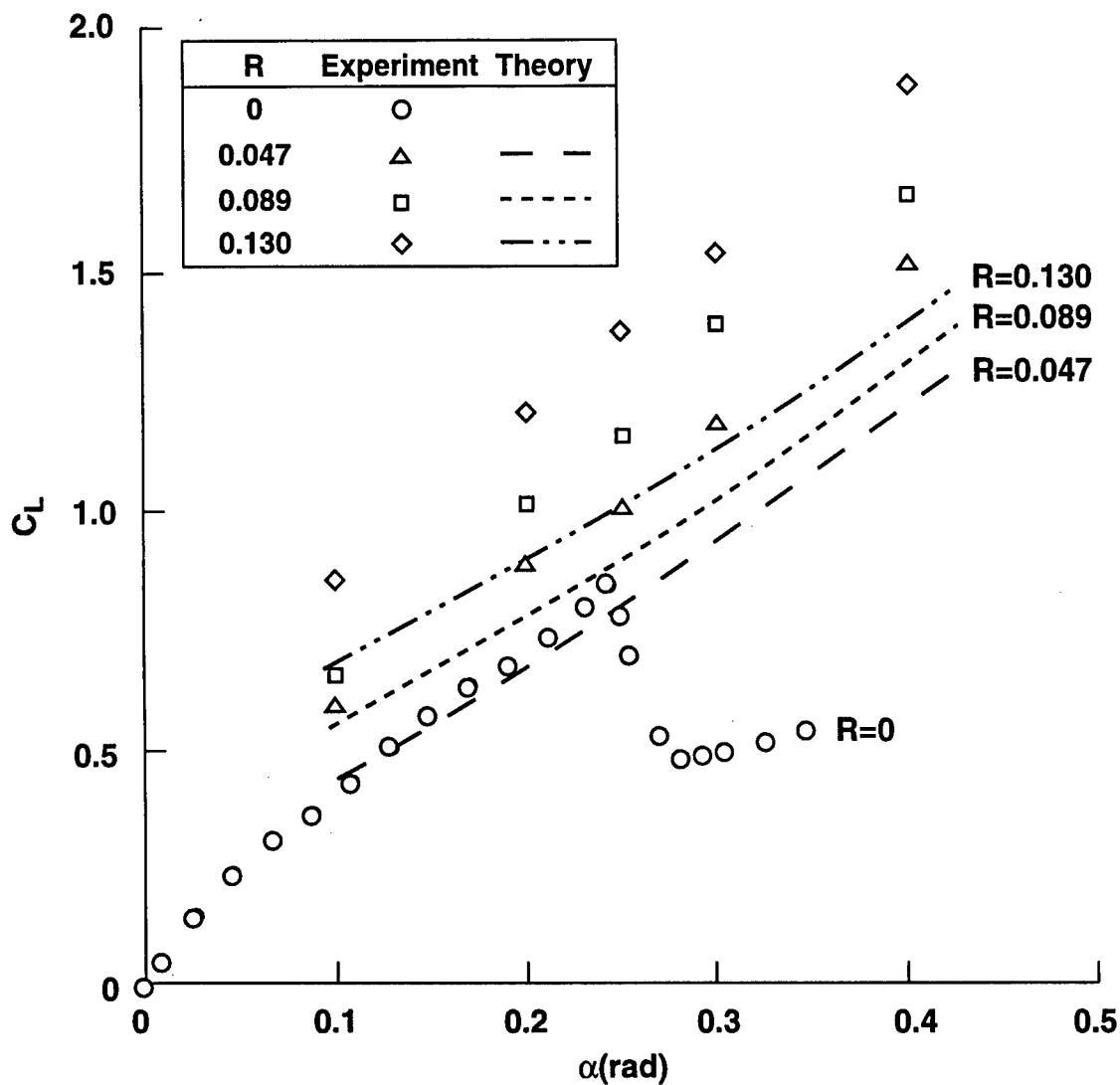


Fig. 16. Computed C_L (Eq. 22) including both circulatory and non-circulatory contributions vs. measurements

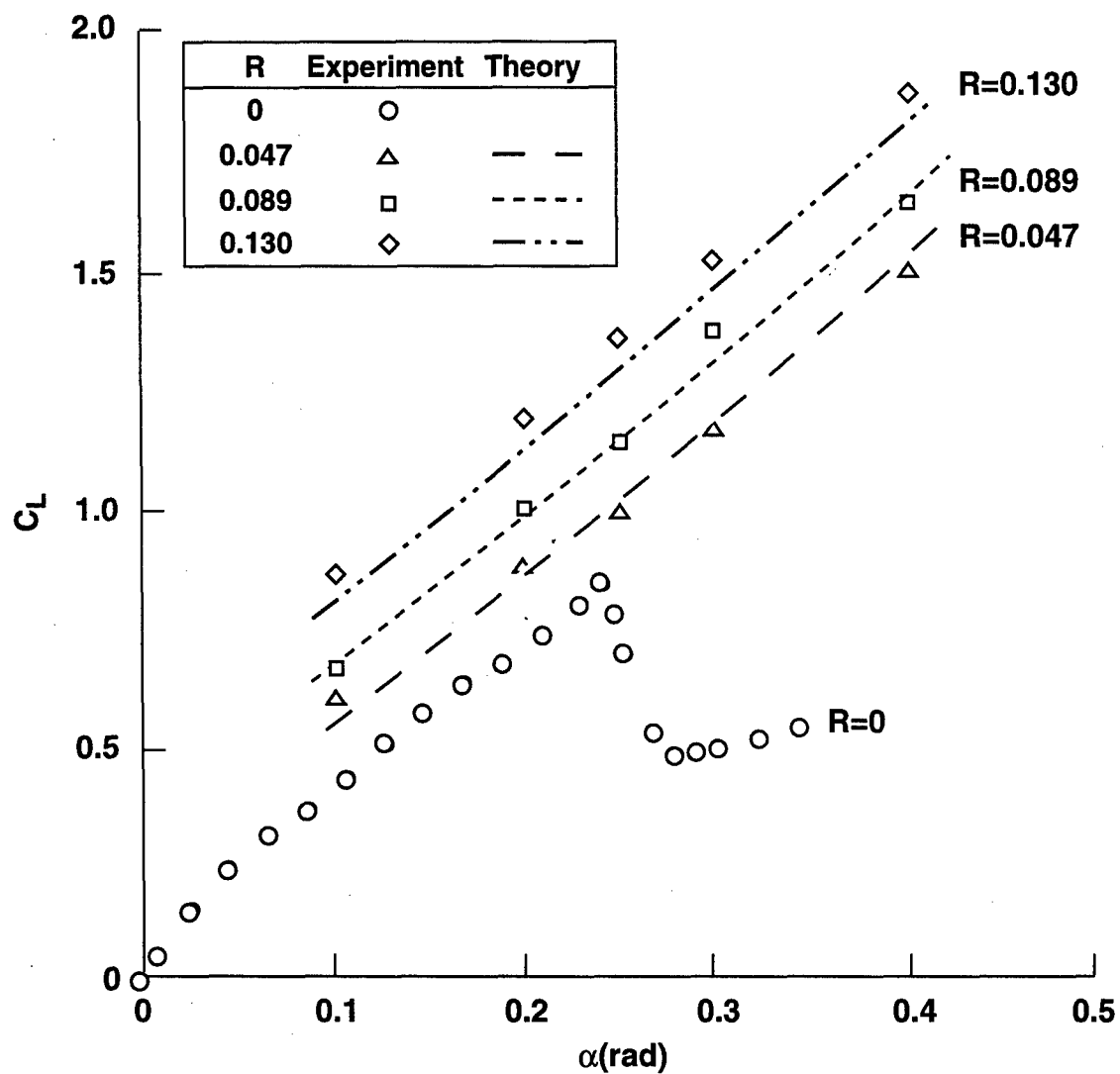


Fig. 17. Computed noncirculatory C_L with $\alpha_w = 0$ vs. measurements

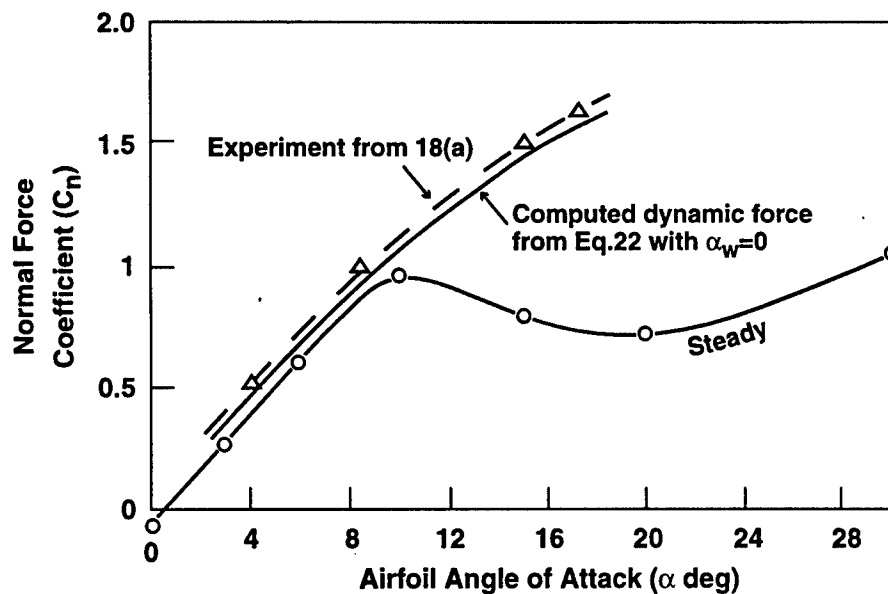
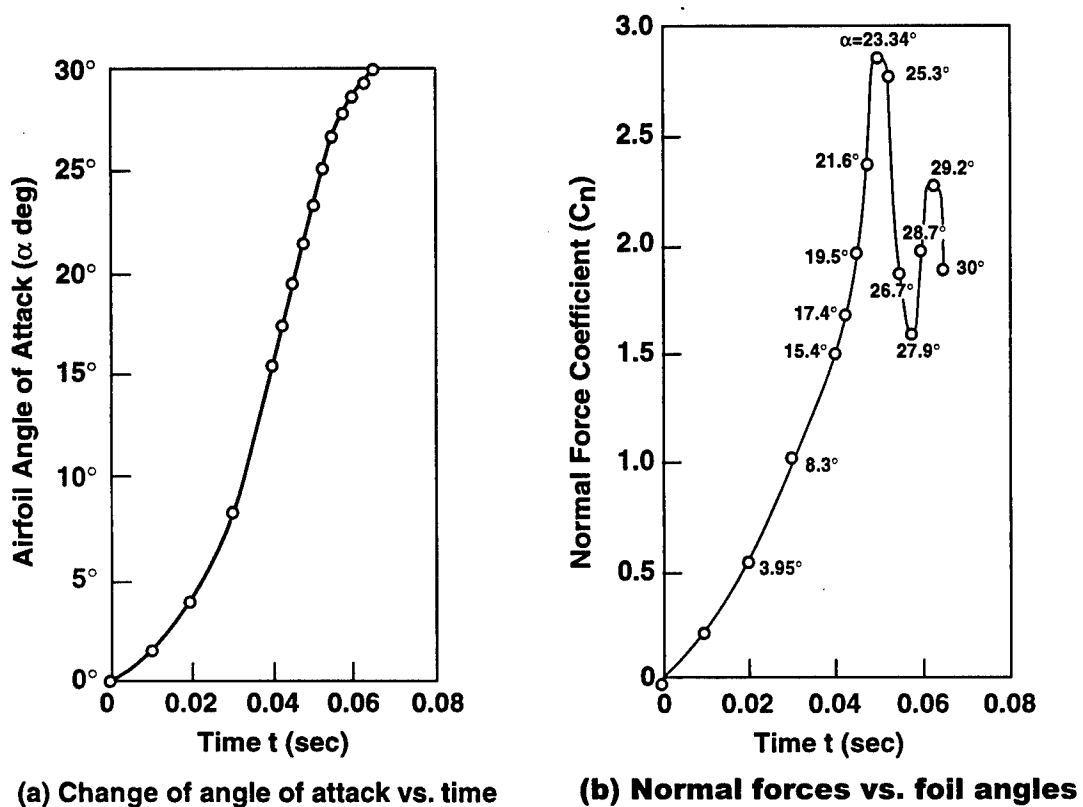
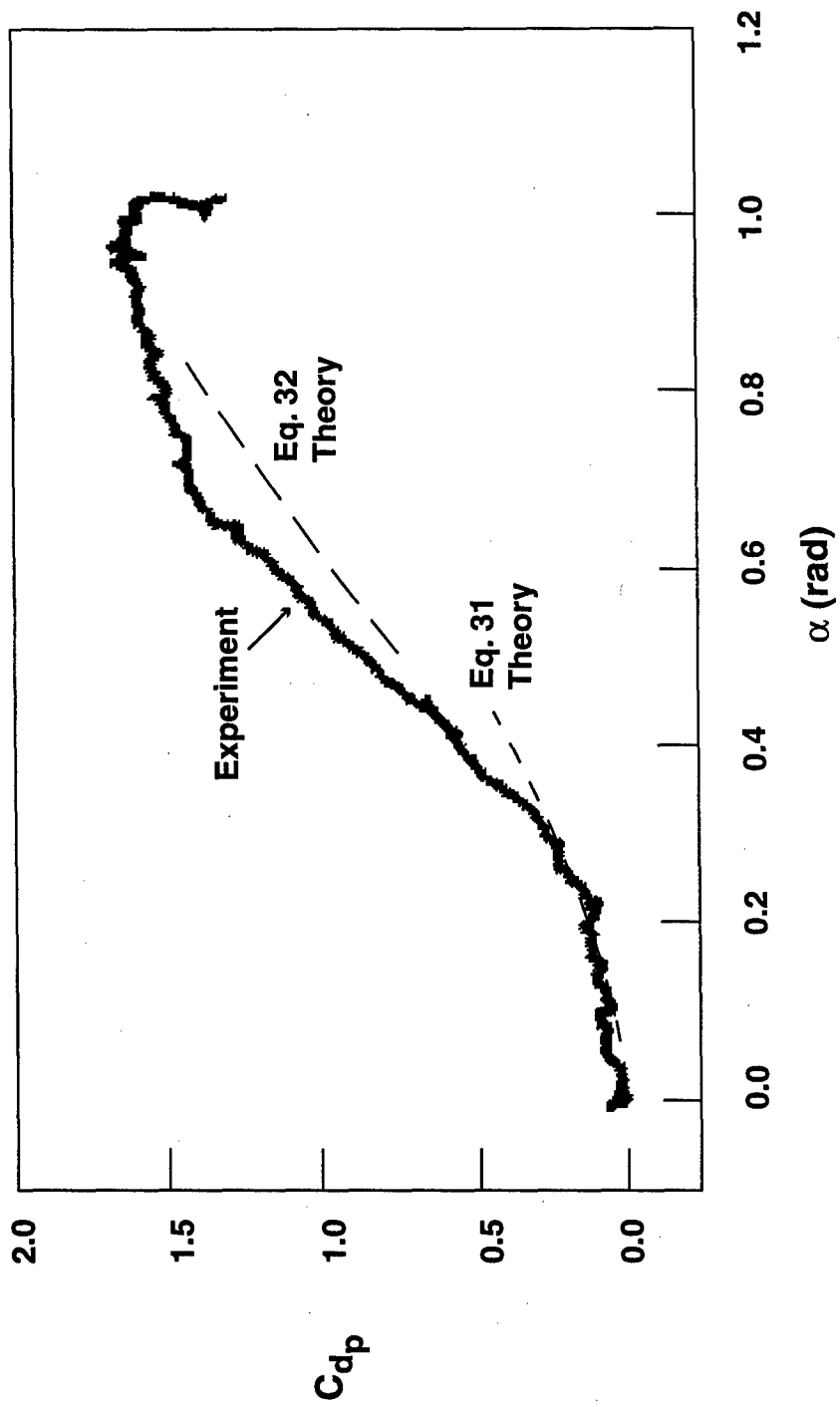
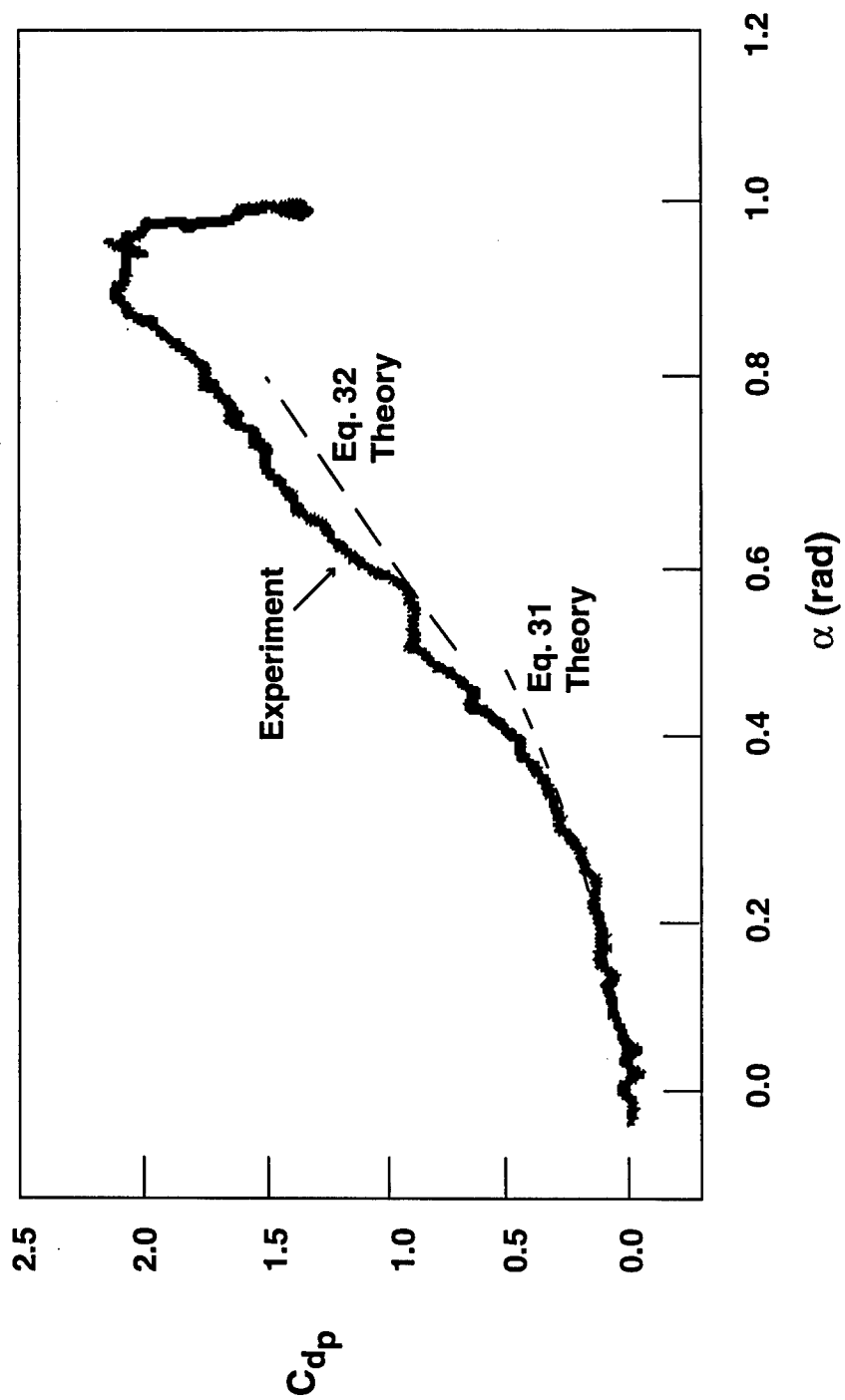


Fig. 18. Ramp tests by Ham (Ref. 23).



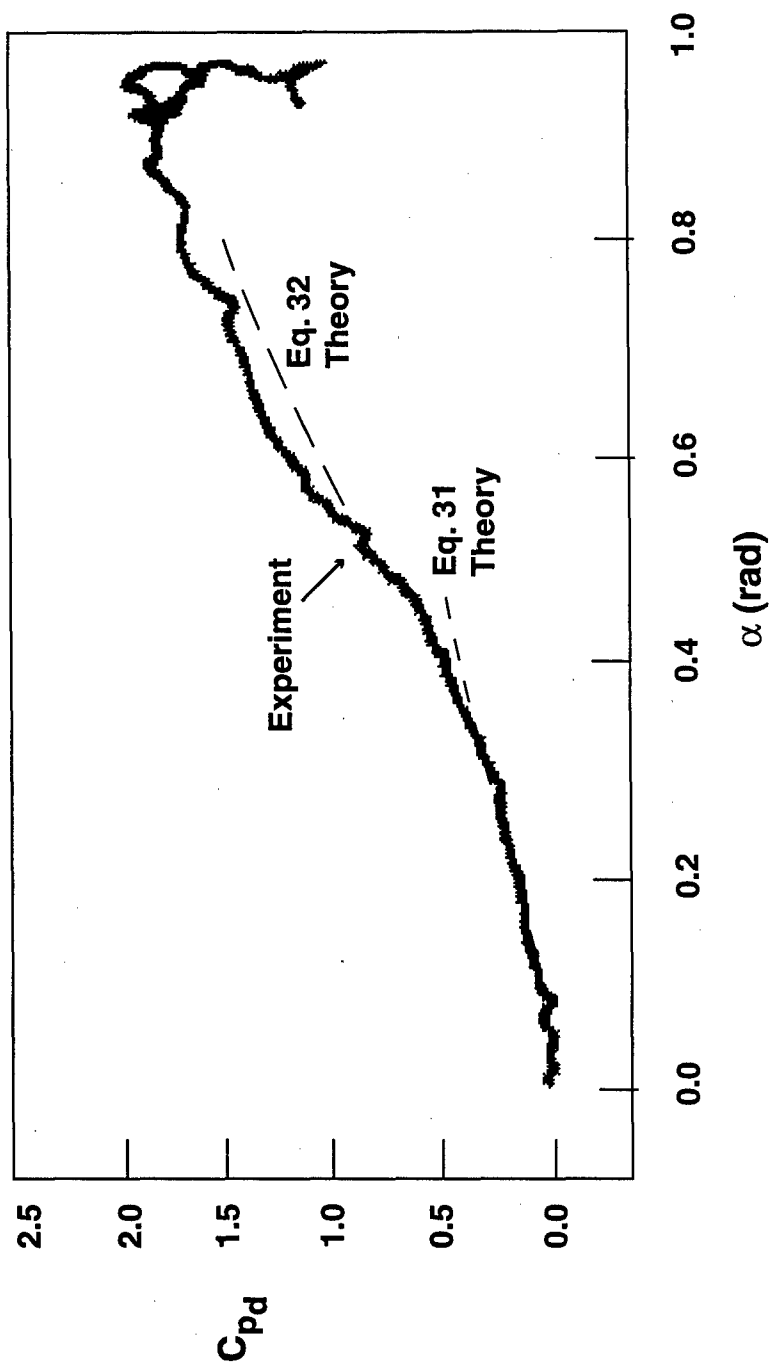
(a) $R=0.047$

Fig. 19. Unsteady effects on drag force.



(b) $R=0.089$

Fig. 19. (Continued)



(c) $R=0.130$

Fig. 19. (Continued)

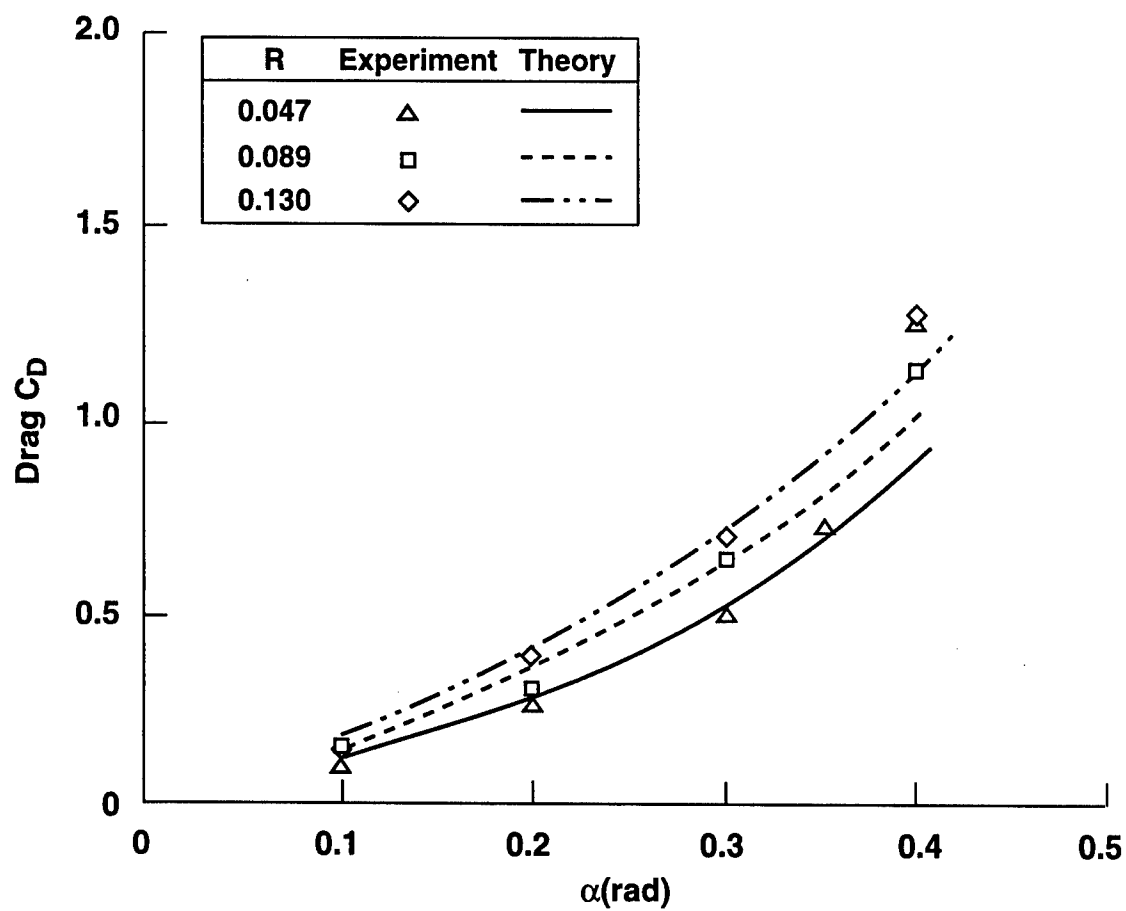
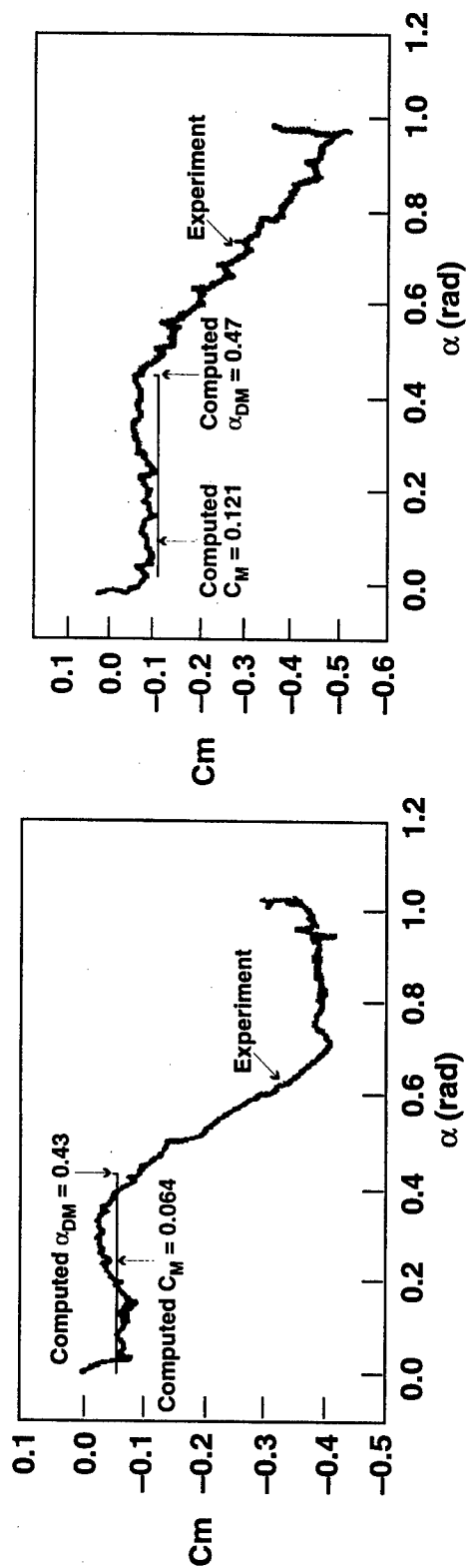


Fig. 20. Unsteady effects on drag, theory vs. experiments.



(b) $R=0.089$

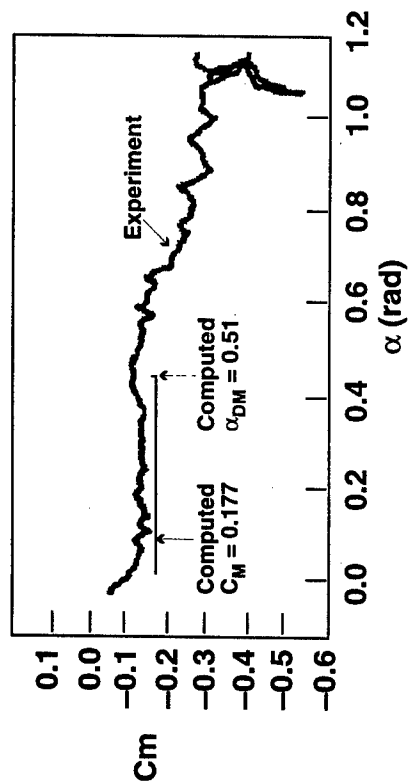


Fig. 21. Unsteady effects on pitch moment, theory vs. measurements in fully attached flow

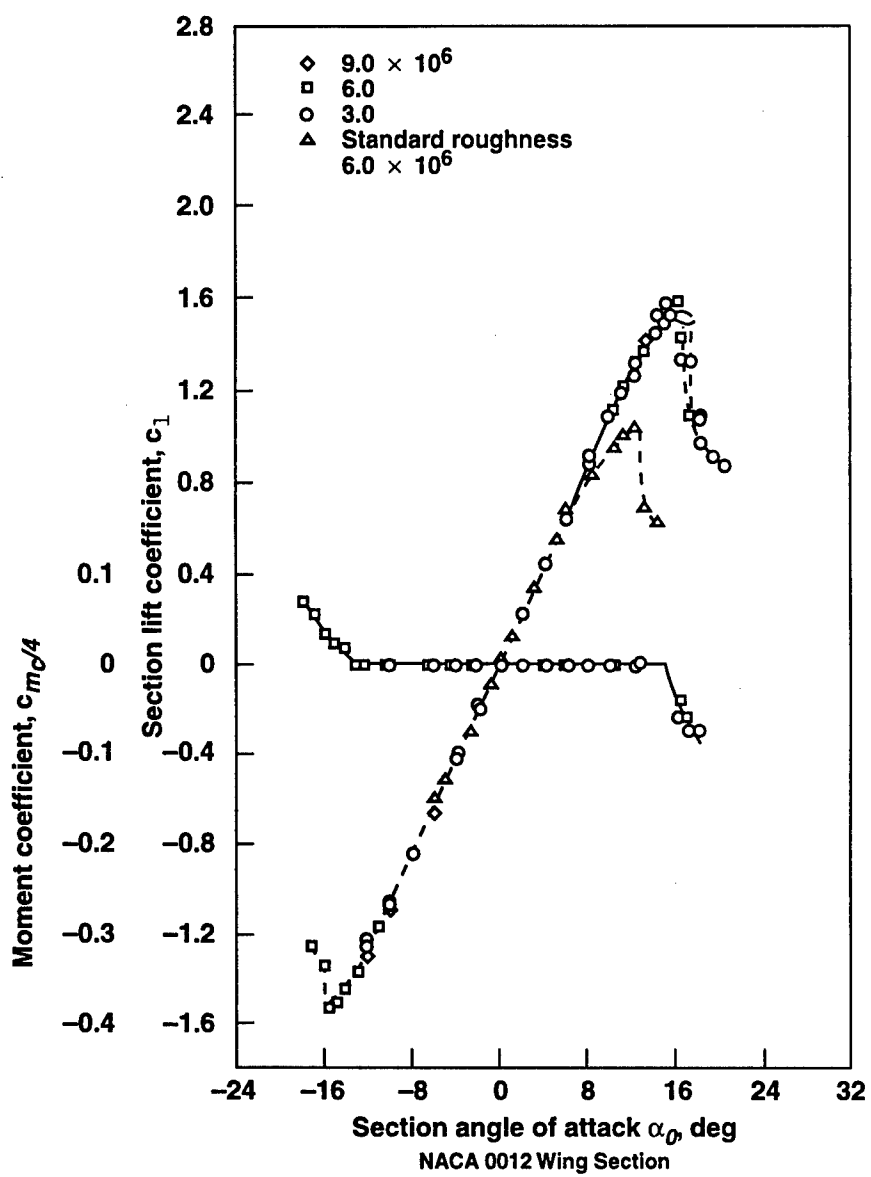


Fig. 22. Steady section force characteristics of NACA 0012 wing section.

REFERENCES

- 1 Clark, D. R., and F. Zhang, "Marine Application User's Manual for the 'Stand Alone' Propeller Force Module (PFM)", AMI Report No. 9608 (August 1996).
- 2 Drela, Mark, "XFOIL: An Analysis and Design System for Low Reynolds Number Airfoils", Low Reynolds Number Aerodynamics, Springer-Verlag Lec. Notes in Eng. 54 (1989).
- 3 Critzos, C. C., H. H. Heyson, and R. W. Boswinkle, "Aerodynamic Characteristics of NACA 0012 Airfoil Section at Angles of Attack from 0 to 180," NACA Technical Note 3361 (1955).
- 4 Shen, Y.T., and D. Fuhs, "Blade Section Lift Coefficients for Propellers at Extreme Off-Design Conditions", Report CRDKNSWC/HD-1205-02 (December 1997).
- 5 Leishman, J. G. and T. S. Beddoes, "A Semi-Empirical Model for Dynamic Stall," J. of the American Helicopter Society, pp 3-17 (July 1989).
- 6 Leishman, J. G., "Two-Dimensional Model for Airfoil Unsteady Drag Below Stall," J. of Aircraft, Vol 25, pp. 665-666 (July 1998).
- 7 Abbott I. H. and A. E. von Doenhoff, Theory of Wing Sections, Dover Publications, Inc, New York (1959).
- 8 Wagner, H., "Über die Entstehung des Dynamischen Auftriebes von Tragflugeln," Zeitschrift für Angewandte Mathematik und Mechanik, Bd 5, Heft 1 (Feb. 1925).
- 9 Ericsson, L. E., and J.P. Reding, "Dynamic Stall of Helicopter Blades," J. of American Helicopter Society, Vol 17, pp.11-19 (January 1972).
- 10 Farren, W. S., "The Reaction on a Wing Whose Angle of Incidence is Changing Rapidly," A.R.C. R&M No.1648 (January 1935).
- 11 Theodorsen, T., "General Theory of Aerodynamic Instability and the Mechanism of Flutter," NACA Report 496 (1935).
- 12 Sears, W. R., "Operational Methods in the Theory of Airfoils in Non-uniform Motion, J. of the Franklin Institute, Vol. 230, pp.95-111 (1940).
- 13 Kussner, H. G., "Zusammenfassender Bericht über den Instationären Auftrieb on Flugeln," Luftfahrtforschung, Vol. 13, No. 12 (1936).
- 14 Bisplinghoff R., H. Ashley, and R. Halfman, Aeroelasticity, Addison-Wesley (1955).
- 15 Beddoes, T. S., "A Synthesis of Unsteady Aerodynamic Effects Including Stall Hysteresis," Vertica, Vol. 1, pp. 113-123 (1976).
- 16 Gangwani, S. T. , "Synthesized Airfoil Data Method for Prediction of Dynamic Stall and Unsteady Airloads," Proceedings of the 39th Annual Forum of the American Helicopter Society (1983).
- 17 McLaughlin, T. E., "Aerodynamic Foundations for Use of Unsteady Aerodynamic Effects in Flight Control," Ph.D. Dissertation, University of Colorado (1992).

- 18 Francis, M. S., and J. E. Keesee, "Airfoil Dynamic Stall Performance with Large Amplitude Motions," AIAA Journal, Vol. 23, pp.1653-1659 (Nov. 1985).
- 19 McCroskey, W. J., et al, "Dynamic Stall on Advanced Airfoil Sections," J. of American Helicopter Society, Vol. 26, No. 3, pp.40-50 (July 1981).
- 20 McCroskey, W. J., "The Phenomenon of Dynamic Stall," NASA TM 81264 (March 1981).
- 21 Johnson, W., "A Comprehensive Analytical Model of Rotorcraft Aerodynamics and Dynamics," Camrad/JA User Manual, Johnson Aeronautics, Palo Alto, Ca.
- 22 Green, R., and R. A. Galbraith, "A Demonstration of the Effect of the Testing Environment on Unsteady Aerodynamics Experiments," Aeronautical Journal (March 1994).
- 23 Ham, N. D., and M. S. Garelick, "Dynamic Stall Considerations in Helicopter Rotors," J. of American Helicopter Society, Vol. 13, No. 2, pp.49-55 (April 1968).
- 24 Kottapalli, S. B., and G. A. Pierce, "Drag on an Oscillating Airfoil in a Fluctuating Free Stream," J of Fluids Engineering, Vol. 101, pp.113-123 (Sept. 1979).